Chapter 4

Structure-Induced Ultratransparency in Photonic Crystals

Jie Luo and Yun Lai

Additional information is available at the end of the chapter

http://dx.doi.org/10.5772/intechopen.71274

Abstract

This chapter presents the recent progress on structure-induced ultratransparency in both one- and two-dimensional photonic crystals (PhCs). Ultratransparent PhCs not only have the omnidirectional impedance matching with the background medium, but also have the ability of forming aberration-free virtual images. In certain frequency regimes, such ultratransparent PhCs are the most transparent solid materials on earth. The ultratransparency effect has many applications such as perfectly transparent lens, transformation optics (TO) devices, microwave transparent devices, solar cell packaging, etc. Here, we demonstrate that the ultratransparent PhCs with "shifted" elliptical equal frequency contour (EFC) not only provide a low-loss and feasible platform for transformation optics devices at optical frequencies, but also enable new degrees of freedoms for phase manipulation beyond the local medium framework. In addition, microwave transparent devices can be realized by using such ultratransparent PhCs.

Keywords: ultratransparency, photonic crystals, impedance matching, spatial dispersion, transformation optics

1. Introduction

Photonic crystals (PhCs), as periodic arrangement of dielectrics, affect the motion of photons and electromagnetic (EM) waves in much the same way that semiconductor crystals affect the propagation of electrons, providing a new mechanism to control and manipulate the flow of light at wavelength scale [1–5]. The key property of the PhCs is the photonic band gap induced from the periodic modulation of photons and EM waves, which can block wave propagation in certain or all directions. As photonic band-gap materials, PhCs play vital roles in light confinement and optical manipulation, promising many important applications, such as omnidirectional reflectors [6, 7], waveguides [8, 9], fibers [10], high-Q nanocavities and laser [11, 12], and angular filters [13].

However, little attention has been paid to the effect of enhancing transparency. Although there are pass bands in PhCs, they are usually reflective and, therefore, not transparent enough. As we know, transparent media are the foundation of almost all optical instruments, such as optical lens. However, perfect transparency has never been realized in natural transparent solid materials such as glass because of the impedance mismatch with free space. On the other hand, in the past decades, artificial EM materials like metamaterials [14–20] have been proposed to realize unusual EM properties beyond natural materials. However, most of the researches were focused on the realization of abnormal refractive behaviors such as negative refraction. Transparency over a large range of incident angle or a large frequency spectrum is theoretically possible, but the experimental realization is very difficult as complex and unusual parameters are required.

The photonic band-gap effect is actually induced by the periodic modulation of the reflections on the surfaces of dielectrics. That is, the periodic modulation strengthens the reflections on the surfaces of dielectrics to form a complete band gap at particular frequencies. Then, a natural question is: Is it possible to rearrange the periodic modulation of the reflections on the surfaces of dielectrics to make them cancel each other for all incident angles, so that omnidirectional impedance matching and omnidirectional perfect transmission can be realized?

In this chapter, we show the opposite effect of the band-gap effect in PhCs, i.e., the structure-induced ultratransparency effect [21, 22]. Ultratransparent PhCs not only have the omnidirectional impedance matching with the background medium, but also have the ability of forming aberration-free virtual images. The equal frequency contours (EFCs) of such ultratransparent PhCs are designed to be elliptical and "shifted" in the k-space and thus contain strong spatial dispersions and provide more possibilities for omnidirectional impedance matching. Interestingly, the combination of perfect transparency and elliptical EFCs satisfies the essential requirement of ideal transformation optics (TO) devices [23–27]. Therefore, such ultratransparent PhCs not only provide a low-loss and feasible platform for TO devices at optical frequencies, but also enable new freedom for phase manipulation beyond the local medium framework. Moreover, such ultratransparent PhCs have shown enormous potential applications in the designs of microwave transparent wall, nonreflection lens, omnidirectional polarizer, and so on.

2. Ultratransparency effect: the opposite of the band-gap effect

2.1. Definition of ultratransparency: omnidirectional impedance matching and aberration-free virtual image

It is well known that the band-gap effect induced by the periodic distribution of dielectrics can block the propagation of EM waves in certain or all directions, as illustrated in **Figure 1(a)**. The forbiddance of wave propagation is the result of lacking propagation modes within the PhCs, which can be seen from the EFCs in **Figure 1(a)**. The circle in the left denotes the EFC of free space, and there is no dispersion of the PhCs within the band gap. Interestingly, we would like to rearrange the periodic array of dielectrics to obtain the omnidirectional impedance matching effect, which allows near 100% transmission of light at all incident angles, as illustrated in **Figure 1(b)**.

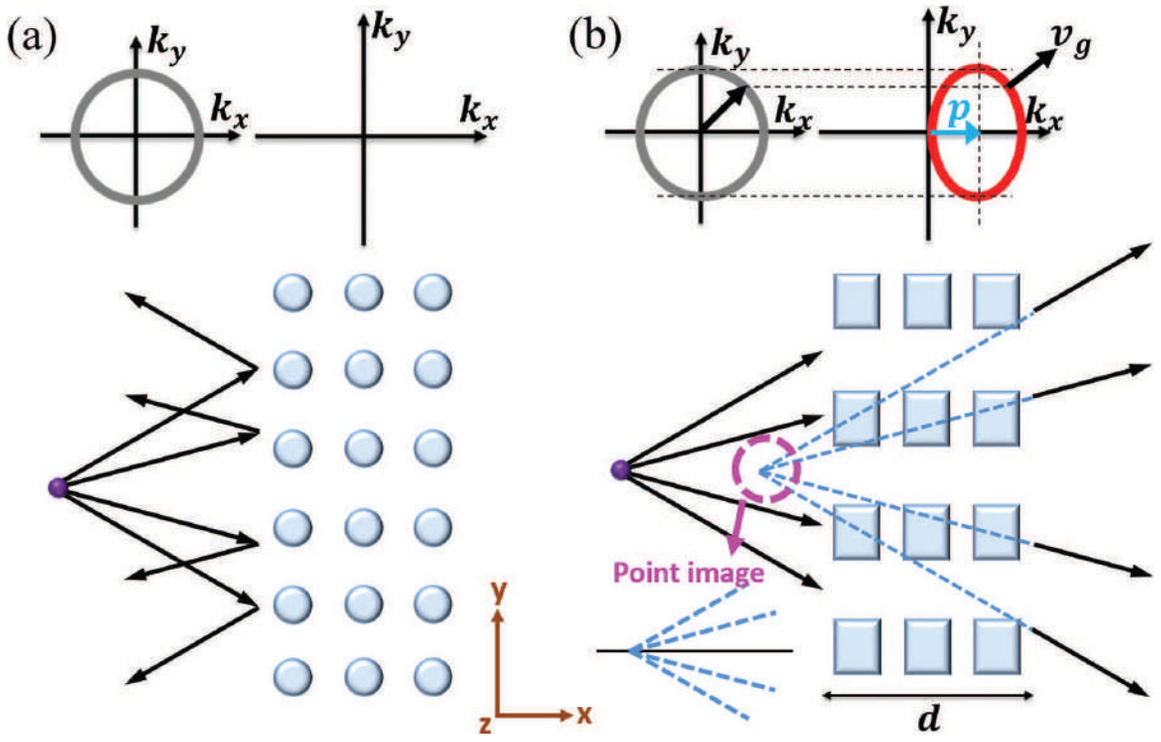

Figure 1. (a) Total reflection by a PhC slab with complete photonic band gap. (b) Aberration-free virtual image formation through an ultratransparent medium without any reflection due to omnidirectional impedance matching. The arrows and dashed lines in (a) and (b) represent the light rays from a point source, and the back-tracing lines, respectively. The inset graphs show the corresponding EFCs.

Moreover, we expect such media to have the ability of forming aberration-free virtual images, which is absent in normal transparent media like glass. By using ray optics, it can be easily shown that transmitted rays from a point source behind a dielectric slab would form a "blurred" area of virtual image rather than a point image. For demonstration, we placed a point source on the left side of a glass slab (with a thickness of d and a refractive index of 1.46) at a distance of d, as shown in **Figure 2(a)**. The virtual image is formed by the back tracing lines (thin lines) of the transmitted waves in the right side (thick lines), showing evident aberrations. In **Figure 2(b)**, we present the zoom in "blurred" image in the region marked by dashed lines in **Figure 2(a)**, showing the spatial distribution of the formed virtual image. This implies that the position of the virtual image will change if we observe from different positions, as illustrated in **Figure 2(c)**.

Actually, such aberrations of the virtual image originate from the mismatch between the EFCs of free space and dielectrics, i.e., their EFCs do not have the same height in the transverse direction (i.e., the k_y direction in **Figure 1**) [21]. By using ray optics, it can be demonstrated that a circle or elliptical EFC having the same height of the EFC of free space in the k_y direction enables the formation of aberration-free virtual images [21], i.e., the EFC has the form of

$$\frac{(k_x - p)^2}{q} + k_y^2 = k_0^2, \tag{1}$$

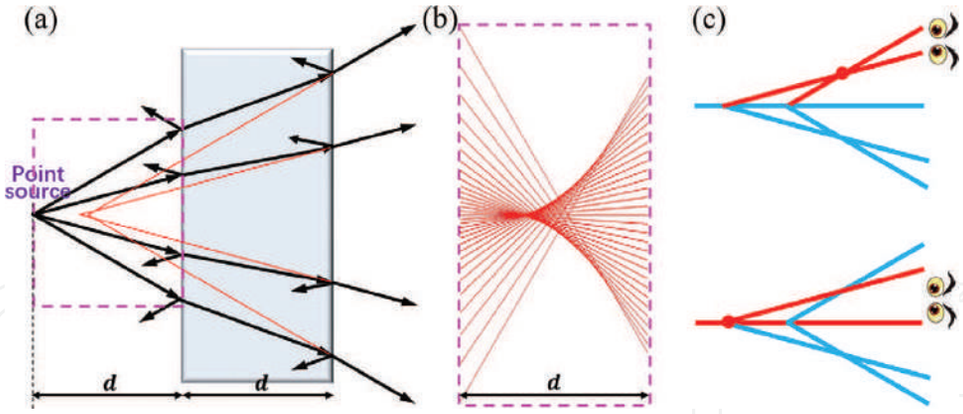

Figure 2. The formation of "blurred" virtual image by a glass slab. (a) The existence of general reflection and aberration in virtual images behind a glass slab. (b) The zoom in "blurred" image in the region marked by dashed lines in (a). (c) The position of the virtual image for the observation from different positions.

where k_0 is the wave number in air, $k_{x(y)}$ is the $x(y)$ component of the wave vector, p denotes the displacement from the Brillouin zone center, and q determines the ratio of the k_y and k_x axes of the ellipse, as shown in **Figure 1(b)**. We note that the "shift" of p in the k_x direction does not affect the formation of virtual images, because such a "shift" does not change the refractive behavior at all in this case.

Supposing that the rearrangement of the periodic array of dielectrics not only makes the whole structure impedance matched to free space for all incident angles, but also creates the unique EFC described by Eq. (1); thus, both omnidirectional 100% perfect transmission and aberration-free virtual imaging are enabled simultaneously. Apparently, such a level of transparency is superior to that of normal transparent media like dielectrics and is thus hereby denoted as ultratransparency.

2.2. Ultratransparency based on local and nonlocal media

According to Fresnel equations, reflection of light on the surface of dielectrics is inevitable, except at a single-incident angle referred to as the Brewster angle under transverse magnetic (TM) polarization, as demonstrated in **Figure 3(a)**. Here, we extend the impedance matching from one particular angle (i.e., Brewster angle) to all incident angles in a nonlocal or spatial dispersive medium, whose effective permittivity $\boldsymbol{\varepsilon}(k_y)$ and permeability $\boldsymbol{\mu}(k_y)$ are dependent on wave vectors.

To begin with, we assume that the nonlocal medium exhibits an irregular-shaped EFC shown in **Figure 3(b)**. An incident wave of transverse electric (TE) polarization with electric fields polarized in the z direction is considered. For the TE polarization, the dispersion relation of the nonlocal medium can be expressed in a general form as,

$$\frac{k_x^2}{\mu_y(k_y)} + \frac{k_y^2}{\mu_x(k_y)} = \varepsilon_z(k_y)k_0^2, \tag{2}$$

which determines the relationship between the components of wave vectors k_x and k_y.

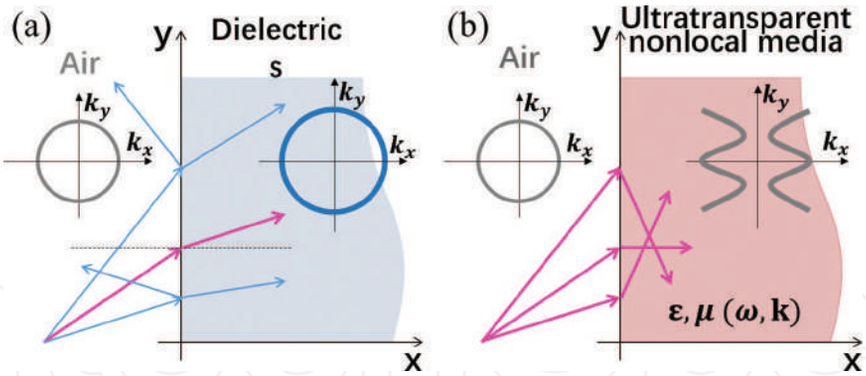

Figure 3. (a) There exist reflected waves at the interface of free space and dielectrics except for the Brewster angle for TM polarization. (b) Nonreflection and total transmission on the surface of ultratransparent nonlocal media for all incident angles. The thin circle, thick circle, and curves in the inset graphs denote the EFCs of air, dielectrics, and the nonlocal media, respectively.

In this case, the wave impedance of free space can be derived as $Z_0 \equiv \frac{E_z}{H_y} = -\frac{\mu_0}{k_{x,0}}\omega$ for TE polarization [28–30]. E_z and H_y are the z-component of electric fields and the y-component of magnetic fields, respectively. $k_{x,0}$, μ_0, and ω are the x-component of wave vector in free space, the permeability of vacuum, and angular frequency of the EM wave, respectively. Similarly, the wave impedance of the nonlocal medium can be written as $Z = -\frac{\mu_0\mu_y(k_y)}{k_x}\omega$. Then, the impedance matching of the nonlocal medium and free space requires $Z = Z_0$. By considering dispersion relations, the impedance matching condition is obtained as,

$$\frac{\mu_x(k_y)\mu_y(k_y)}{\mu_x(k_y)\varepsilon_z(k_y)k_0^2 - k_y^2} = \frac{1}{k_0^2 - k_y^2} \tag{3}$$

If Eq. (3) can be satisfied for all $|k_y| < k_0$, then omnidirectional impedance matching can be achieved, leading to near 100% transmission of light for all incident angles.

An obvious local medium solution of Eq. (3) is that $\mu_x\mu_y = 1$ and $\mu_x\varepsilon_z = 1$, which correspond to elliptical EFCs centered at the Brillouin zone center, are consistent with transformation optics theory [23–27]. However, this is not the only possible solution for spatially dispersive media. Now, we consider medium with the EFC described by Eq. (1), i.e., $k_x = p \pm \sqrt{q\left(k_0^2 - k_y^2\right)}$. By substituting this relation into Eq. (3) and the spatial dispersion, we obtain the analytical forms of spatially dispersive parameters as:

$$\mu_y^2(k_y) = \frac{\left[p \pm \sqrt{q\left(k_0^2 - k_y^2\right)}\right]^2}{k_0^2 - k_y^2} \text{ and } \varepsilon_z(k_y)k_0^2 - \frac{k_y^2}{\mu_x(k_y)} = \pm\left[p \pm \sqrt{q\left(k_0^2 - k_y^2\right)}\right]\sqrt{k_0^2 - k_y^2} \tag{4}$$

Eq. (4) shows that when EM parameters possess spatial dispersions, there exist infinite solutions of $\mu_y(k_y)$, $\varepsilon_z(k_y)$, and $\mu_x(k_y)$ for the satisfaction of Eq. (4) for all $|k_y| < k_0$, indicating infinite solutions for omnidirectional impedance matching.

3. Structure-induced ultratransparency in two-dimensional PhCs

3.1. Nonlocal effective medium theory

For the design of ultratransparent PhCs, we first propose a nonlocal effective medium theory for the homogenization of PhCs. Here, we consider uniform plane wave incidence. In this situation, the validity of the nonlocal effective medium theory lies in the satisfaction of the following four premises: (1) single-mode approximation [28], i.e., only one eigen-mode is excited; (2) the amplitudes of fields at the incident boundary are almost constant; (3) the phases of fields at the incident boundary obey the trigonometric functions; and (4) the electric and magnetic fields are in phase at the incident boundary. Although these premises are seemingly stringent, it turns out that most eigen-modes of the first few bands (e.g., monopolar and dipolar bands) can indeed satisfy these requirements (**Figure 4**).

With the assumption of the abovementioned premises, eigen-fields of TE polarization at the boundary $x = 0$ can be approximately expressed as $\mathbf{F} = \mathbf{F}_0 e^{i(k_x x + k_y y)} e^{-i\omega t}$ with $\mathbf{F}_0 = E_0\hat{z}, H_0\hat{y}$. E_0 and H_0 are the amplitudes of eigen-electric and eigen-magnetic fields, respectively, which are almost independent of y. This indicates that the eigen-fields are the boundary and have the same formula as those in a uniform medium. Thus, the surface impedance of the PhCs can be calculated in a similar formula as [28–30],

$$Z_x = \frac{\langle E_z \rangle_{x=0}}{\langle H_y \rangle_{x=0}} \text{ and } Z_y = \frac{\langle E_z \rangle_{x=0}}{\langle H_x \rangle_{x=0}} \tag{5}$$

where $\langle F \rangle_{x=0}$ denotes the average of eigen-field F along the unit cell boundary $x = 0$. E_z, H_x and H_y are the z-component of eigen-electric fields, x- and y-components of eigen-magnetic fields, respectively. Based on Eq. (5), the surface impedance of a PhC can be calculated as long as the eigen-fields of the PhC are solved.

On the other hand, the PhC satisfying previous premises generally can be described as a uniform medium with effective relative permittivity $\begin{pmatrix} \varepsilon_{x,eff} & & \\ & \varepsilon_{y,eff} & \\ & & \varepsilon_{z,eff} \end{pmatrix}$, relative

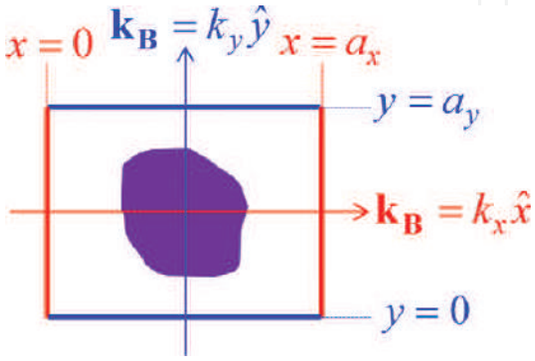

Figure 4. Schematic graph of the unit cell for the nonlocal effective medium theory.

permeability $\begin{pmatrix} \mu_{x,eff} & & \\ & \mu_{y,eff} & \\ & & \mu_{z,eff} \end{pmatrix}$, and dispersion $\frac{k_x^2}{\mu_{y,eff}} + \frac{k_y^2}{\mu_{x,eff}} = \varepsilon_{z,eff} k_0^2$. Thus, the impedance of the PhC can be rewritten as the function of effective parameters:

$$Z_x = -\frac{\mu_0 \mu_{y,eff}}{k_x}\omega \text{ and } Z_y = \frac{\mu_0 \mu_{x,eff}}{k_y}\omega \tag{6}$$

Compared with Eqs. (5) and (6), the effective parameters can be derived as,

$$\begin{aligned} \varepsilon_{z,eff} &= \frac{1}{\varepsilon_0 \omega}\frac{k_y \langle H_x \rangle_{x=0} - k_x \langle H_y \rangle_{x=0}}{\langle E_z \rangle_{x=0}}, \\ \mu_{x,eff} &= \frac{k_y}{\mu_0 \omega}\frac{\langle E_z \rangle_{x=0}}{\langle H_x \rangle_{x=0}} \text{ and } \mu_{y,eff} = -\frac{k_x}{\mu_0 \omega}\frac{\langle E_z \rangle_{x=0}}{\langle H_y \rangle_{x=0}} \end{aligned} \tag{7}$$

With Eq. (7), the effective parameters of the PhC can be obtained by analyzing the eigen-fields with Bloch wave vector $\mathbf{k_B} = k_x\hat{x} + k_y\hat{y}$. We note that the Bloch wave vector is restricted in the first Brillouin zone, and the choice of the eigen-fields of $-\mathbf{k_B}$ or $+\mathbf{k_B}$ depends on the direction of group velocity. In addition, we find that this method is still valid even for the eigen-modes far away from the Brillouin center, but the effective parameters are generally k-dependent, i.e., nonlocal or spatially dispersive.

3.2. Two-dimensional ultratransparent PhCs

PhCs contain strong spatial dispersions and thus provide the perfect candidate for realization of ultratransparency effect. Here, we demonstrate a type of PhCs composed of a rectangular array of dielectric rods in free space, with the unit cell shown in **Figure 5(a)**. Under TE polarization, the band structure is presented in **Figure 5(b)**, and the EFC of the third band is plotted in the reduced first Brillouin zone in **Figure 5(c)**. The working frequency is chosen as $fa/c = 0.3183$, where f, a, and c are the frequency, the lattice constant, and the speed of light in free space, respectively. We see that the corresponding EFC (the right dashed lines in **Figure 5(c)**) is indeed a "shifted" ellipse that can be described by Eq. (1) with $p \approx \pi/a$. And the dispersion can be approximately written as,

$$\left(\frac{k_x - \pi/a_1}{0.4541a_2/0.5097a_1}\right)^2 + k_y^2 = \left(\frac{0.5097\pi}{a_2}\right)^2 \tag{8}$$

Figure 5(d) shows the impedance difference of the PhC and free space of the third band, i.e., $\left|\frac{Z-Z_0}{Z+Z_0}\right|$, where Z is the impedance of the PhC obtained from Eq. (5) and Z_0 is the impedance of free space. From **Figure 5(d)**, it is seen that the impedance difference is very small for a very large range of k_y at the working frequency, indicating impedance matching in a large range of incidence angles.

Moreover, in **Figure 6(a)**, we present the effective parameters $\varepsilon_{z,eff}$ (square dots), $\mu_{x,eff}$ (circular dots), and $\mu_{y,eff}$ (triangular dots) of the PhC based on Eq. (7), showing the k-dependence.

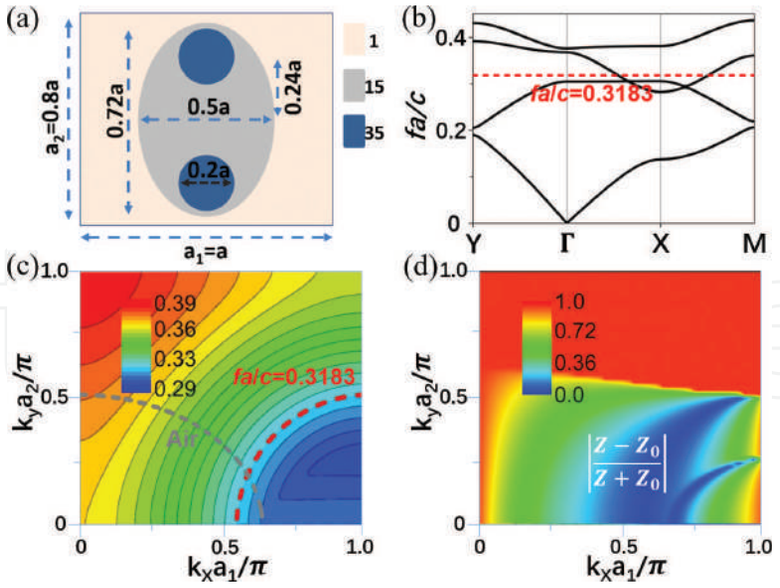

Figure 5. (a) Illustration of the unit cell of the ultratransparent PhC. (b) The band structure of the PhC. The dashed line denotes the working frequency $fa/c = 0.3183$. (c) The EFC of the third band. The left and right dashed lines denote the EFCs of air and the PhC at the frequency $fa/c = 0.3183$. (d) The impedance difference of the PhC and free space of the third band. Reprinted (figure) with permission from Ref. [21]. Copyright (2016) by the American Physical Society.

Interestingly, we find $\mu_{x,eff} \approx 1$, while $\varepsilon_{z,eff}$ and $\mu_{y,eff}$ are both dependent on k_y. The result of $\mu_{x,eff} \approx 1$ can be physically understood. Since the resonances are localized in the dielectrics and far away from the incident boundary, the modes propagating in the y direction are weakly modulated by the periodicity. As a consequence, $\mu_{x,eff}$ has the same value as the relative permeability of the background medium.

Now, by substituting the condition $\mu_{x,eff} \approx 1$ and the dispersion Eq. (8) into Eq. (4), the analytical form of the effective parameters $\varepsilon_{z,eff}$ and $\mu_{y,eff}$ can be solved as,

$$\varepsilon_{z,eff}(k_y) = \pm\frac{\pi}{a_1 k_0^2}\left[1 - 0.4541\sqrt{1-\left(\frac{k_y a_2/\pi}{0.5097}\right)^2}\right]\sqrt{k_0^2 - k_y^2} + \frac{k_y^2}{k_0^2}$$
$$\text{and } \mu_{y,eff}(k_y) = \pm\frac{\pi}{a_1}\left[1 - 0.4541\sqrt{1-\left(\frac{k_y a_2/\pi}{0.5097}\right)^2}\right]/\sqrt{k_0^2 - k_y^2} \tag{9}$$

The choice of $\pm k_x$ depends on the direction of group velocity. Here, we choose $-k_x$, because hereby the band branch in the region $-\pi/a_1 < k_x < 0$ in the first Brillouin zone is excited, as determined by the direction of group velocity. In **Figure 6(a)**, $\varepsilon_{z,eff}$ and $\mu_{y,eff}$ based on Eq. (9) (dashed lines) show perfect match with those obtained from Eq. (7) for all $k_y < k_0$, demonstrating the omnidirectional impedance matching effect.

For further verification, the transmittance through such a PhC slab consisting of N (= 4, 5, 6, 15) layers of unit cells in the x direction is numerically calculated, as presented in **Figure 6(b)**. It is shown that the transmittance is near unity (>99%) for nearly all incident angles ($\theta < 89^\circ$) and is

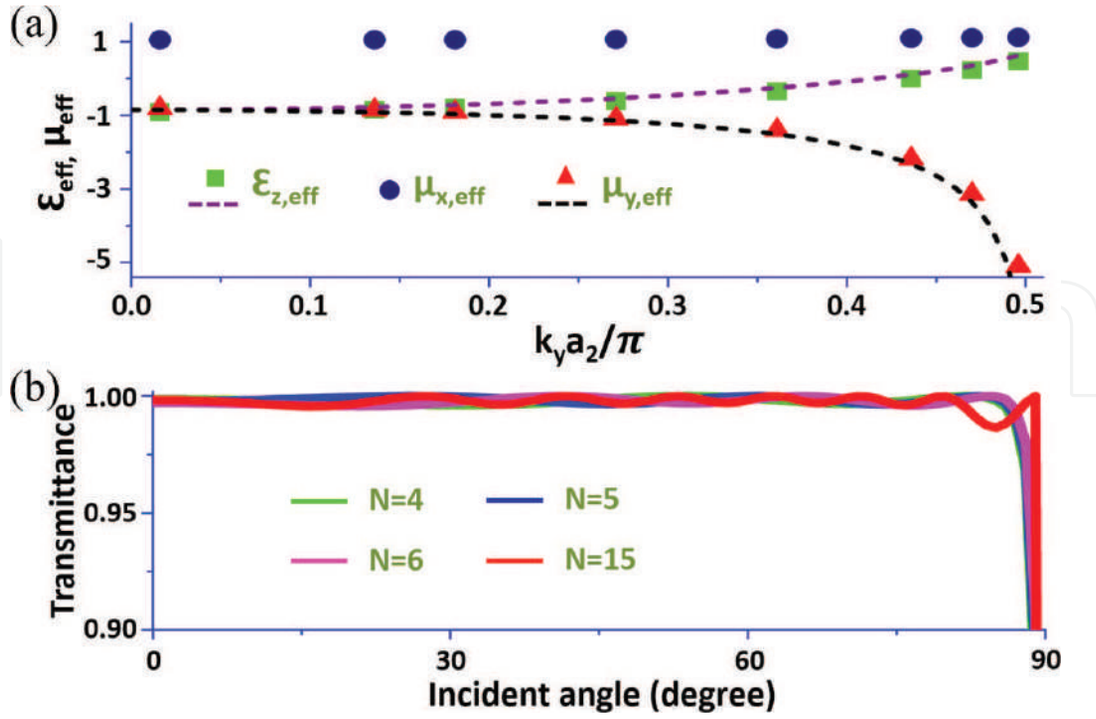

Figure 6. (a) The effective parameters $\varepsilon_{z,eff}$, $\mu_{x,eff}$, and $\mu_{y,eff}$ retrieved from the eigen-fields based on Eq. (7) (symbols) and predicted by the ultratransparency condition based on Eq. (9) (dashed lines). (b) Calculated transmittance through a PhC slab with N (= 4, 5, 6, 15) layers of unit cells as the function of incident angles. Reprinted (figure) with permission from Ref. [21]. Copyright (2016) by the American Physical Society.

almost irrespective of the layer number N, indicating that the total transmission is a result of impedance matching instead of tunneling effects.

3.3. Microwave experimental verification

In fact, for transparency in a relatively smaller range of incident angles, the design process is much easier and the effect can exist in much simpler structures. In the following, we demonstrate a simple ultratransparent PhC, which is verified by proof-of-principle microwave experiments. The PhC consists of rectangular alumina ($\varepsilon = 8.5$) bars in a square lattice, as illustrated by the inset in **Figure 7(a)**. The lattice constant is set to be a = 12 mm, and the length (W_1) and width (W_2) are 9.6 mm and 4.8 mm, respectively, corresponding to 0.8a and 0.4a. We consider TE polarization with electric fields polarized along the z direction, and the band structure is presented in **Figure 7(a)**. The normalized frequency is chosen to be $fa/c = 0.4723$ (marked by a dashed line), corresponding to a working frequency around 11.8 GHz. In **Figure 7(b)**, we can see that the shape of EFC of $fa/c = 0.4723$ is nearly a part of "shifted" ellipse. And the dispersion can be approximately written as,

$$\left(\frac{k_x - \pi/a_1}{0.4541a_2/0.5097a_1}\right)^2 + k_y^2 = \left(\frac{0.5097\pi}{a_2}\right)^2 \tag{10}$$

In addition, the impedance difference between the PhC and the free space is calculated by using Eq. (5), as shown in **Figure 7(c)**. Clearly, the impedance difference is very small on the

EFC of $fa/c = 0.4723$ for a large range of k_y, demonstrating the wide-angle impedance matching effect.

Moreover, the effective parameters obtained from Eq. (7) are presented in **Figure 8(a)** by solid lines with symbols, showing $\mu_{x,eff} \approx 1$ for $k_y < 0.818\pi/a$ as the result of weakly modulated

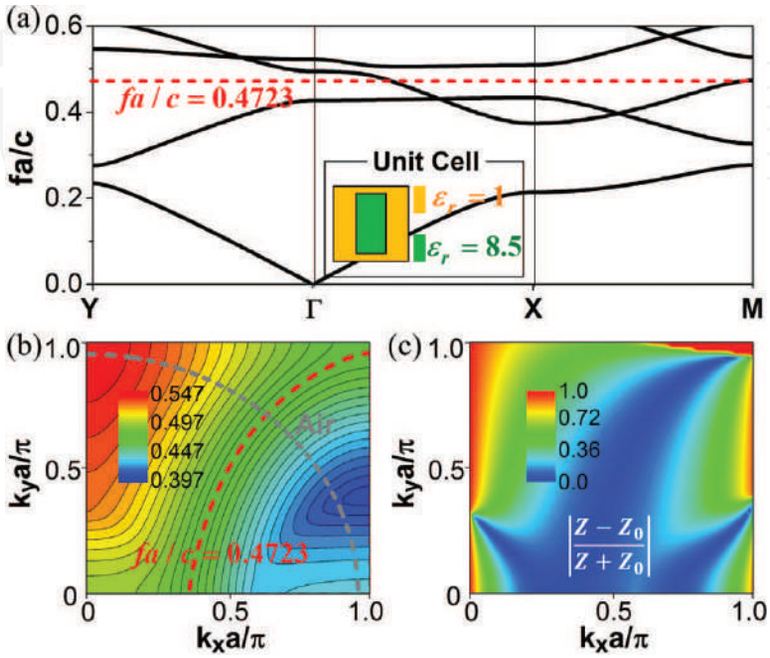

Figure 7. (a) Band diagram of the experimental PhC for TE polarization. The dashed line denotes the working frequency $fa/c = 0.4723$. The inset is the illustration of the unit cell of the PhC. (b) EFCs in the frequency range $0.397 \le fa/c \le 0.547$. The left and right dashed lines denote the EFCs of air and the PhC at the frequency $fa/c = 0.4723$. (c) The impedance difference of the PhC and the free space in the frequency range $0.397 \le fa/c \le 0.547$.

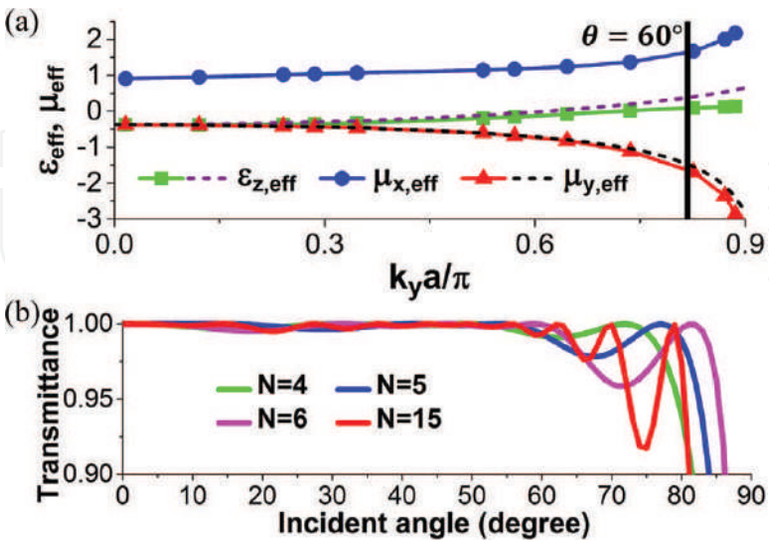

Figure 8. (a) Effective parameters $\varepsilon_{z,eff}$, $\mu_{x,eff}$, and $\mu_{y,eff}$ retrieved from the eigen-fields based on Eq. (7) (solid lines with symbols) and predicted by the ultratransparency condition based on Eq. (11) (dashed lines). (b) Transmittance through a N (= 4, 5, 6, 15)-layered PhC slab as the function of incident angles.

modes propagating in the y direction. By inserting the condition $\mu_{x,eff} \approx 1$ and the dispersion Eq. (10) into Eq. (4), the analytical expressions of $\varepsilon_{z,eff}$ and $\mu_{y,eff}$ can be derived as,

$$\begin{cases} \varepsilon_{z,eff}(k_y) = \pm\dfrac{\pi}{ak_0^2}\left[1.25 - 0.8945\sqrt{1-\left(\dfrac{k_y a/\pi}{1.0415}\right)^2}\right]\sqrt{k_0^2 - k_y^2} + \dfrac{k_y^2}{k_0^2} \\ \mu_{y.eff}(k_y) = \pm\dfrac{\pi}{a}\left[1.25 - 0.8945\sqrt{1-\left(\dfrac{k_y a/\pi}{1.0415}\right)^2}\right]/\sqrt{k_0^2 - k_y^2} \end{cases} \tag{11}$$

In **Figure 8(a)**, the dashed lines denote $\varepsilon_{z,eff}$ and $\mu_{y,eff}$ based on Eq. (11) (negative sign is chosen), showing excellent coincidence with those from Eq. (7) for $k_y < 0.818\pi/a$ (i.e., $\theta < 60^\circ$).

Furthermore, we calculate the transmittance through the PhC slab with N (= 4, 5, 6, 15) unit cells, as shown in **Figure 8(b)**. It is clearly seen that there exists near-unity transmittance for all

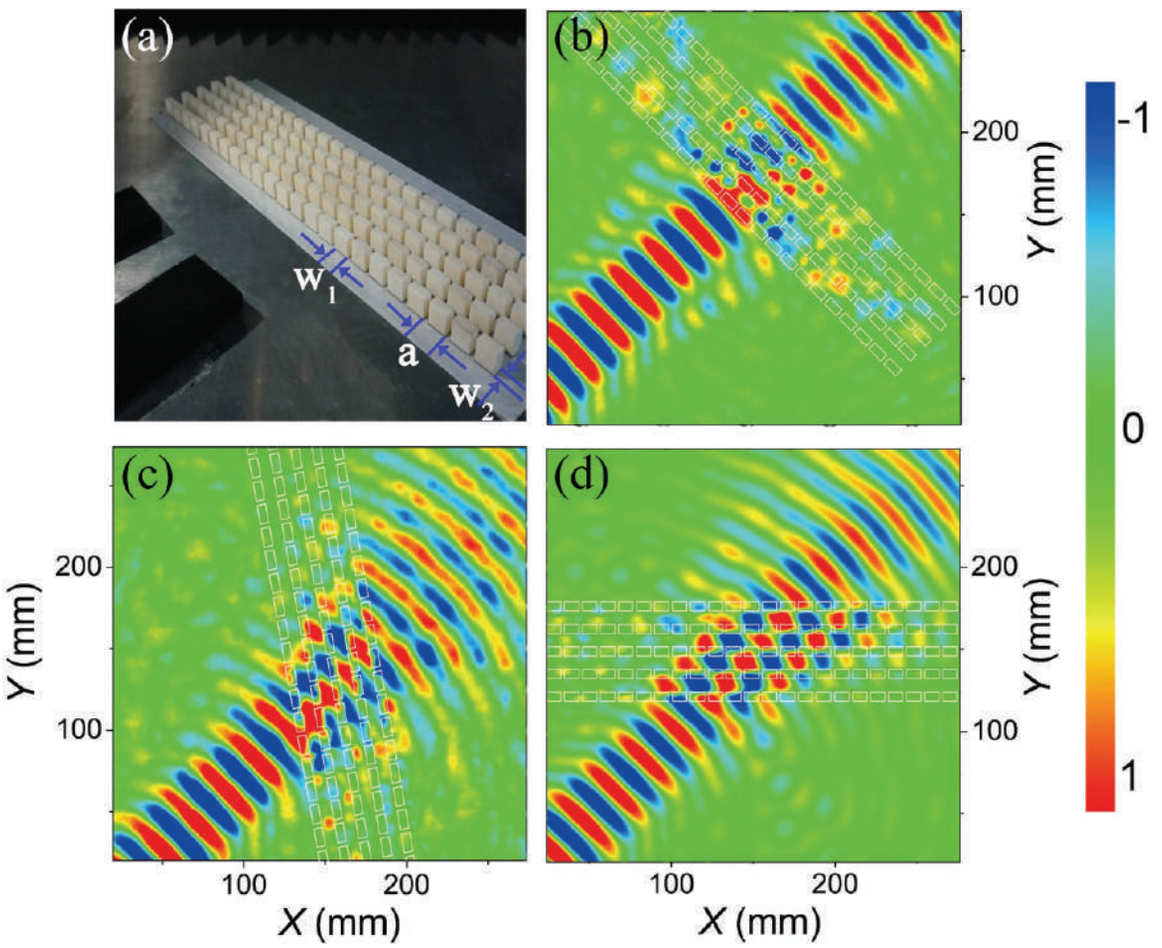

Figure 9. (a) Photo of the PhC composed of alumina bars (white) placed inside the microwave field mapper. The measured electric-field distributions for microwave beams with incident angles of (b) 0°, (c) 30°, and (d) 45°. Reprinted (figure) with permission from Ref. [21]. Copyright (2016) by the American Physical Society.

incident angles of $\theta < 60^\circ$ (i.e., $k_y < 0.818\pi/a$) irrespective of N, demonstrating the wide-angle impedance matching effect.

Next, we show microwave experimental results to verify the above theory. A 23×5 array of such a PhC is assembled in the xy plane inside a parallel-plate waveguide composed of two flat aluminum plates, as shown in **Figure 9(a)**. The separation between the two aluminum plates is 10.5 mm, slightly larger than the height of the bars (10 mm), but smaller than half of the wavelength of interest (25.4 mm for 11.8 GHz) to make sure that the whole experimental chamber can only support transverse EM modes. A microwave beam with a finite width was launched through a waveguide made of absorbing materials (in black in **Figure 9(a)**). The lower metal plate along with the PhC array was mounted on a translational stage. The electric field was measured via an antenna fixed in a hole in the upper metal plate (not shown here). Both the emitting and probing antennas are connected to our Agilent E5071C network analyzer to acquire the transmitted magnitude and phase of microwave signals. Such a setup allows us to measure the spatial distributions in the xy plane for a series of incident angles from 0° to 60° at the working frequency of 11.8 GHz.

The measured electric fields for 0°, 30°, and 45° incident angles are displayed in **Figure 9(b), (c)**, and **(d)**, respectively. Clearly, the reflection is barely noticeable, indicating impedance matching for all these incident angles. In **Figure 10**, the measured transmittance (triangular dots) coincides with simulation results (solid lines) quite well, both showing great enhancement compared with that through an alumina slab with the same thickness (dashed lines). Although the ultratransparency effect is hereby only verified at the microwave frequency regime, the principle can be extended to optical frequency regime by using PhCs composed of silicon or other dielectrics.

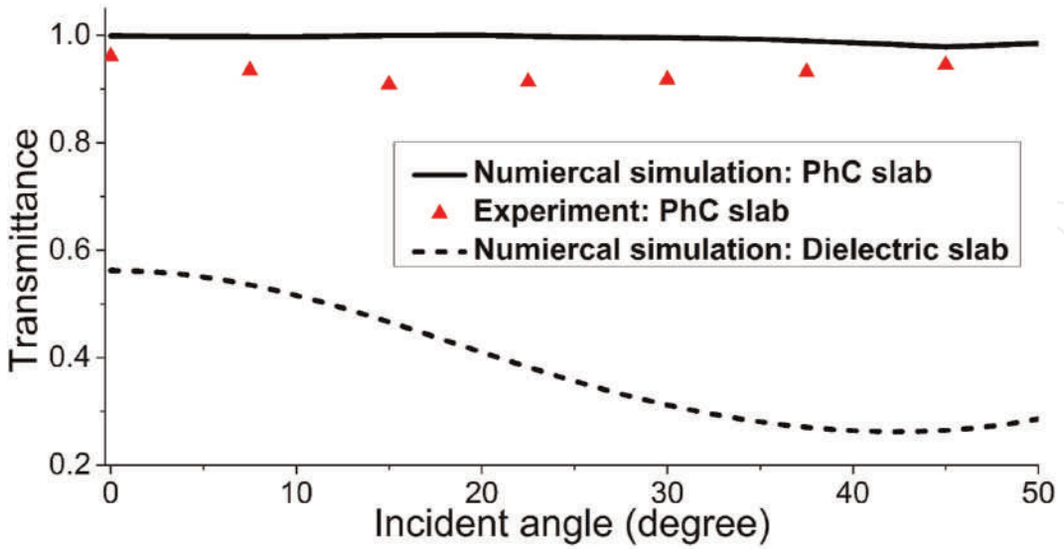

Figure 10. Transmittance through the PhC slab in simulations (solid lines) and experiments (triangular dots) and an alumina slab having the same thickness (dashed lines) as the function of incident angles. Reprinted (figure) with permission from Ref. [21]. Copyright (2016) by the American Physical Society.

4. Structure-induced ultratransparency in one-dimensional PhCs

In the above, we have shown the structure-induced ultratransparency in two-dimensional PhCs. In the following, we demonstrate the structure-induced ultratransparency in one-dimensional PhCs [22].

The one-dimensional ultratransparent PhC we studied is composed of two dielectric materials A and B stacked along the x direction (**Figure 11(c)**). As we know, neither the dielectric material A nor B is perfectly transparent due to impedance mismatch. As a result, a large amount of EM waves are always reflected at the surface of dielectrics, as illustrated in **Figure 11 (a)** and **(b)**. Interestingly, when we periodically stack the two dielectric slabs with appropriate filling ratio and lattice constant, the reflection waves on the dielectrics can cancel each other; thus, wide-angle and even omnidirectional nonreflection can be obtained, as illustrated in **Figure 11(c)**.

Figure 12(a) presents the band structure of the PhC, whose unit cell is constructed in a symmetric form, i.e., ABA structure, as shown by the inset in **Figure 12(a)**. The relative permittivity and filling ratio of the material A (B) are 2 (6) and 0.6 (0.4), respectively. The dashed line denotes the normalized frequency $fa/c = 0.397$, which is chosen as the working frequency.

In **Figure 12(b)** and **(d)**, the EFCs at the frequency $fa/c = 0.397$ for the TE and TM polarizations are plotted, respectively. It is seen that the EFCs can be approximately regarded as a part of an ellipse with the center located at the X point. In addition, the impedance difference between the PhC and air is shown in **Figure 12(c)** (for the TE polarization) and **Figure 12(e)** (for the TM polarization). It is seen that the impedance difference is very small for a large range of k_y in the

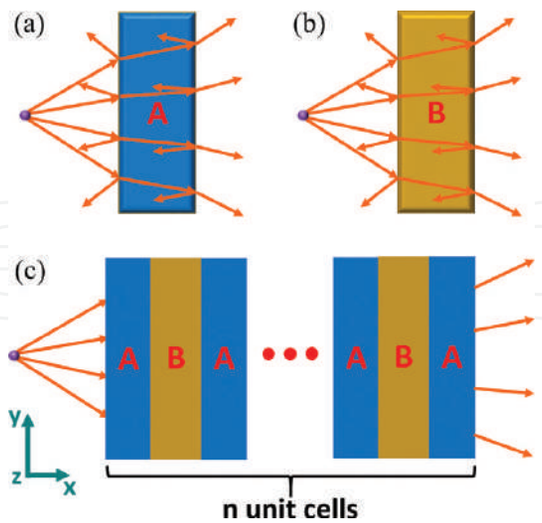

Figure 11. (a) and (b) show general reflection on the slab made of materials A and B, respectively. (c) Elimination of general reflection by a one-dimensional ultratransparent PhC composed of ABA unit cells. The orange arrows represent the rays of light emitted by a point source. Reprinted (figure) with permission from Ref. [22]. Copyright (2016) by the Optical Society.

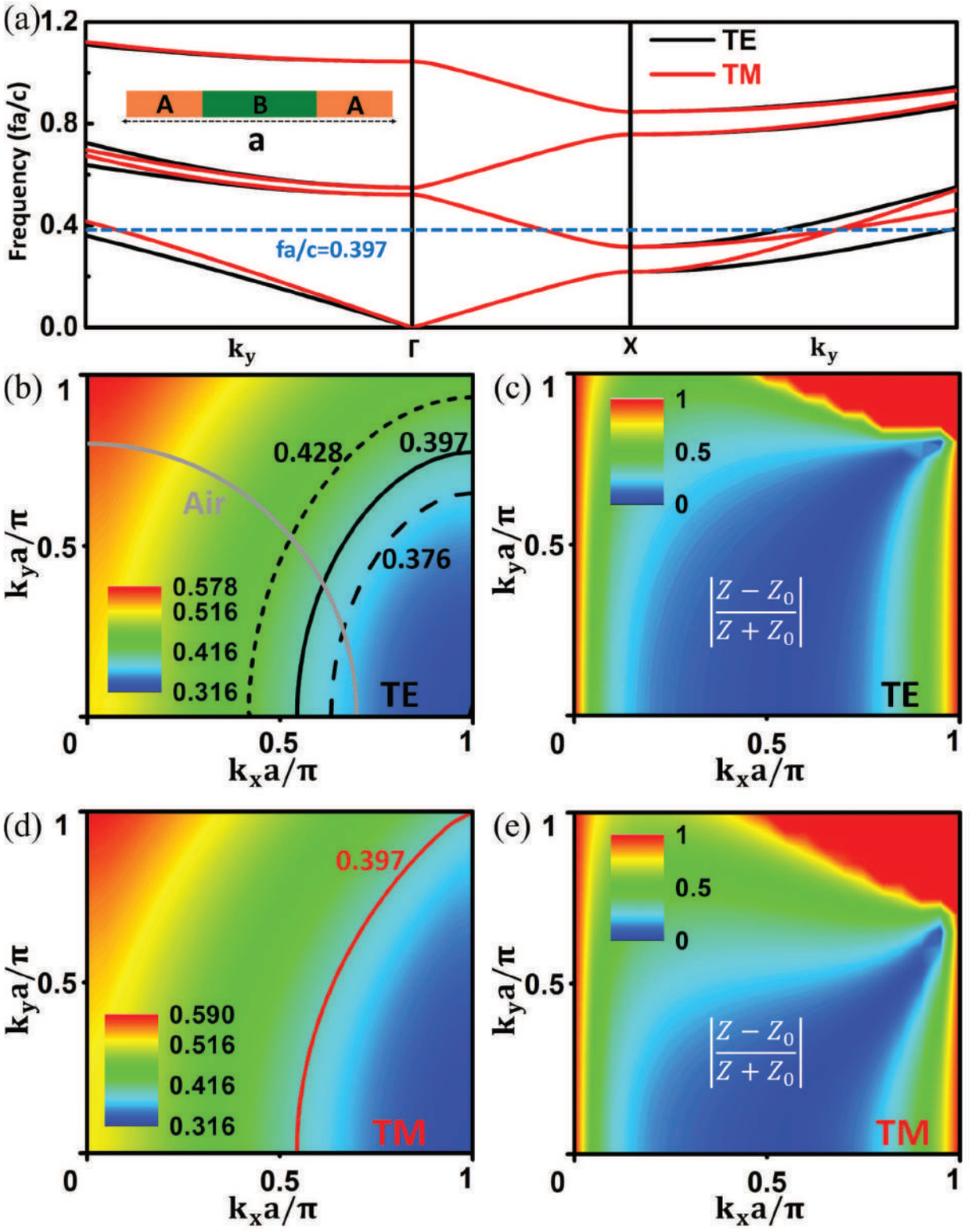

Figure 12. (a) Band structures of the PhC for TE and TM polarizations. The dashed lines denote the working frequency $fa/c = 0.397$. The inset denotes the illustration of the unit cell. (b, d) the EFCs of the PhC and (c, e) the impedance difference between PhC and free space in the second band for (b, c) TE and (d, e) TM polarizations. Reprinted (figure) with permission from Ref. [22]. Copyright (2016) by the Optical Society.

reciprocal space for both polarizations, demonstrating a wide-angle and polarization-insensitive impedance matching effect. Moreover, from **Figure 12(b)** and **(c)**, it is also seen that the impedance difference is small in the frequency range from $fa/c = 0.376$ to $fa/c = 0.428$, indicating a broadband impedance matching effect. Therefore, a one-dimensional PhC exhibiting a broadband, wide-angle, and polarization-insensitive impedance matching effect is realized.

For further verification, the transmittance through the PhC slab composed of N unit cells is calculated. The numerical setup for the transmission computation is shown in **Figure 13(a)**. A TE-polarized plane wave is incident from air in the left side. The upper and lower boundaries are set as periodic boundary condition. From the electric-field distribution in **Figure 13(a)**, we see that almost all the waves can propagate through the PhC slab with 6 unit cells under the incident angle of 45°. In **Figure 13(b)**, the transmittance is plotted as the functions of the incident angle and the number of unit cells (N = 4, 5, 6, 15) for the frequency $fa/c = 0.397$, showing N-independent almost perfect transmission for all incident angles of $\theta < 70°$.

Moreover, in **Figure 14(a)** and **(b)**, the transmittance through a PhC slab ($N = 10$) as the functions of the incident angle and normalized frequency for TE and TM polarizations is presented, which clearly demonstrates the broadband, wide-angle, and polarization-insensitive transparency of the PhC.

Although a wide-angle (0–70°) rather than omnidirectional impedance matching effect is obtained in such a one-dimensional PhC, we may still view such a PhC as an ultratransparent PhC. Compared with the two-dimensional ultratransparent PhCs, the one-dimensional ultratransparent PhCs have the advantages of broadband and polarization-insensitive impedance matching.

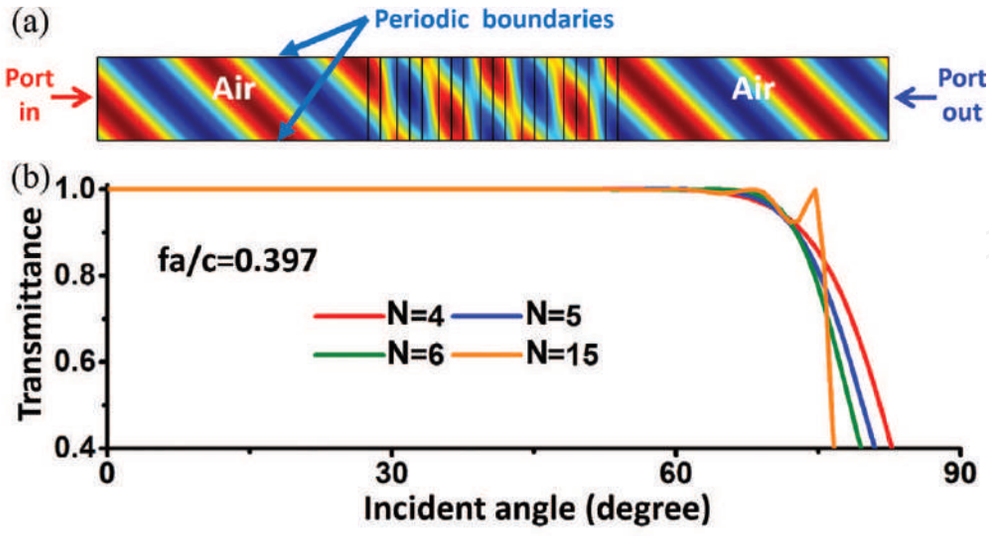

Figure 13. (a) The numerical setup for the transmission computation. The color denotes the distribution of electric fields under $\theta = 45°$ incident angle. (b) Transmittance as the function of the incident angle when EM waves propagate through the PhC slab composed of N (= 4, 5, 6, 15) unit cells. Reprinted (figure) with permission from Ref. [22]. Copyright (2016) by the Optical Society.

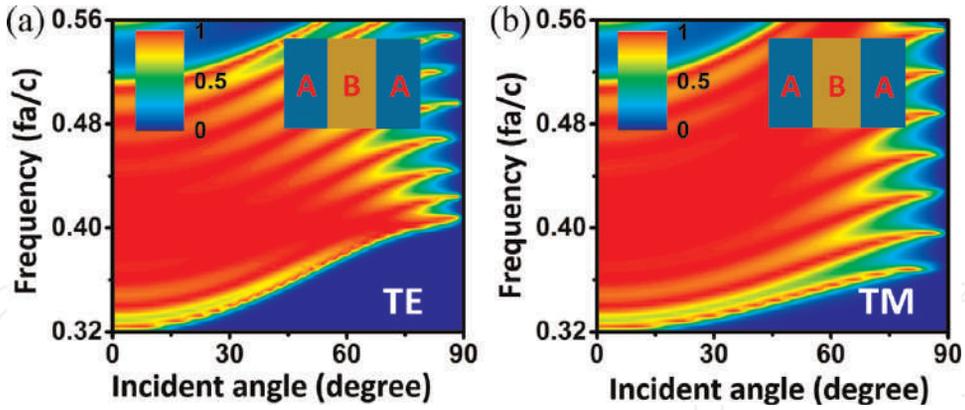

Figure 14. Transmittance as the functions of the incident angle and the frequency for (a) TE- and (b) TM-polarized waves propagating through the PhC slab with 10 unit cells. Reprinted (figure) with permission from Ref. [22]. Copyright (2016) by the Optical Society.

In addition, the easy design and fabrication of the one-dimensional PhCs may lead to more practical applications.

5. Applications

5.1. For transformation optics

In the above, we have demonstrated the ultratransparency in both one- and two-dimensional PhCs. In the following, we show some applications of such ultratransparent PhCs. It is interesting to note that the omnidirectional perfect transparency and elliptical EFCs of the ultratransparent media are essential for ideal TO devices. The theory of TO [23–27] promises many novel and interesting applications, such as invisibility cloaks [23, 25, 31, 32], concentrators [33], illusion optics devices [34–36], and simulations of cosmic phenomena [37, 38]. Generally, the TO devices are realized by using metamaterials [14–20], which require complicated designs of electric and magnetic resonances, hindering the realization and applications in practice. In fact, most of the previous TO experiments were realized by using the so-called reduced parameters, which maintain the refractive behavior, but sacrifice the impedance matching as well as the perfect transparency [25, 39–45]. Moreover, at optical frequencies, the inherent loss in metallic components of metamaterials makes the realization of perfect transparency as well as the ideal nonreflecting TO devices extremely difficult [46, 47], if not impossible. Interestingly, we find that the ultratransparent PhCs provide a low-loss and feasible platform for TO devices at optical frequencies.

To begin with, we consider a TO medium obtained by stretching the coordinate along the x direction in background medium of air. For TE polarization with electric fields polarized in the z direction, the parameters of the TO medium have the relationship [48]:

$$\varepsilon_z = 1/\mu_x = \mu_y = 1/s \tag{12}$$

where s is the stretching ratio. ε_z, μ_x and μ_y are the z component of relative permittivity tensor, x and y components of relative permeability tensor, respectively.

Considering Eq. (12), the dispersion of the TO medium, i.e., $\frac{k_x^2}{\mu_y}+\frac{k_y^2}{\mu_x}=\varepsilon_z k_0^2$, can be rewritten as

$$\frac{k_x^2}{1/s^2}+k_y^2=k_0^2 \tag{13}$$

which has the similar form as that of Eq. (1). The EFC of the TO medium is an ellipse having the same height as the EFC of air in the k_y direction (**Figure 15(a)**), as that of the ultratransparent media. When the stretching ratio is larger than unity, i.e., $s>1$, the EFC of the TO medium (the right ellipse) seems slimmer than the EFC of air (the left circle) in **Figure 15(a),** and the coordinate mesh is looser in the x direction in the TO medium region, as illustrated in **Figure 15(a)**.

The only difference of the EFCs between the TO medium and the ultratransparent medium is that there may exist a "shift" of p in the k_x direction (Eq. (1)) for the ultratransparent medium (**Figure 15(b)**). Interestingly, such a "shift" does not affect the refractive behaviors, but enables new freedom for phase manipulation beyond the local medium framework.

For demonstration, we show a specific example in **Figure 16**. The ultratransparent PhC is one-dimensional and composed of components I and II. The unit cell is constructed in a symmetric way with a lattice constant of a, as illustrated by the inset in **Figure 16(a)**. The relative permittivity and thickness of the component I (II) are 2.132 (5.522) and $0.3a$ ($0.4a$), respectively. In **Figure 16(a)**, the EFC of the PhC at the normalized frequency $fa/c=0.402$ for TE polarization is plotted as the solid lines, which can be viewed as a part of an elliptical located at the X point. Compared with the EFC of the TO medium with $\left\{\varepsilon_z,\mu_x,\mu_y\right\}=\{0.5,2,0.5\}$ (dashed lines in **Figure 16(a)**), we see that the EFC of the PhC has the same height in the k_y direction, which satisfies the requirement proposed above.

Moreover, simulations of wave propagation through the TO medium slab with a thickness of $5a$ (upper inset) and a PhC slab with 5 unit cells (lower inset) are performed, as shown in **Figure 16(b)**.

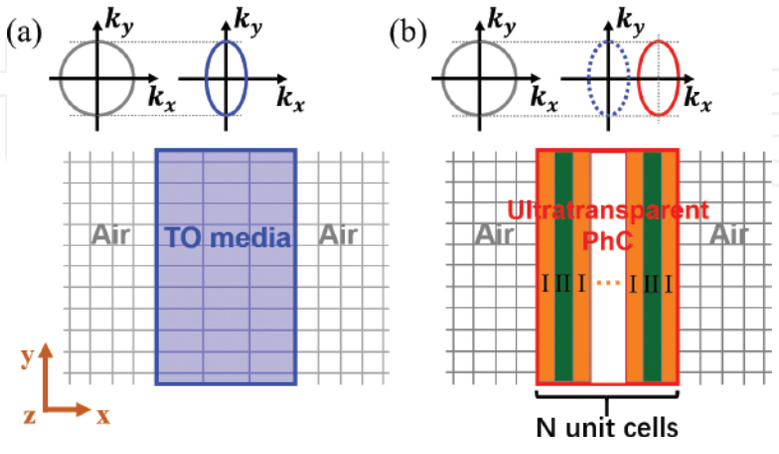

Figure 15. (a) Upper inset: the EFCs of air (the left circle) and TO media obtained by stretching air in the x direction (the right ellipse). Lower inset: scheme of the TO medium slab (with loose mesh) in the background medium of air (with dense mesh). (b) Upper: the EFC of the ultratransparent PhC (the right ellipse with solid lines), which has a "shift" in the k_x direction compared with the EFC of the TO media (dashed lines). Lower inset: the ultratransparent PhC is used to replace the TO medium slab in (a).

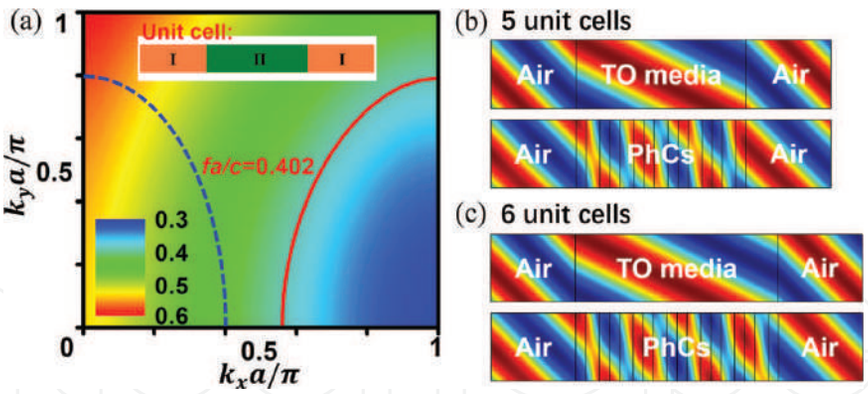

Figure 16. (a) The EFCs of the PhC for TE polarization. The solid line and dashed line denote the EFCs of the PhC and the TO medium at the normalized frequency $fa/c = 0.402$, respectively. (b, c) The snapshot of electric fields for wave propagating through a TO medium slab (upper inset) and a PhC slab (lower inset) under an incident angle of 45°. The thickness of the TO medium slab is (b) 5*a*, (c) 6*a*, and the number of unit cells of the PhC slab is (b) 5, (c) 6.

Simulation results show perfect transmission under the incident angle of 45°. Interestingly, we notice a π phase difference in the transmission waves, which actually is caused by the "shift" of the PhC's EFC and odd number of unit cells. On the other hand, if the total number is even, there will be no phase difference, which is confirmed in the simulation results in **Figure 16(c)**. In **Figure 16(c)**, the thickness of the TO medium slab is 6*a* (upper inset), and the number of unit cells of the PhC slab is 6 (lower inset). Comparing the transmission waves, we see identical phases under the incident angle of 45°. The results demonstrate that the ultratransparent PhC can approximately work as the TO medium with $\left\{\varepsilon_z, \mu_x, \mu_y\right\} = \{0.5, 2, 0.5\}$.

Next, we show an example of TO device by using one-dimensional ultratransparent PhCs. The design process is shown in **Figure 17(a)**, in which the original shell of a concentrator [33] is discretized into four layers and each layer is further replaced by a corresponding ultratransparent PhC. **Figure 17(b)** shows the parameters of the discretized layers of TO media and the ideal profile. The corresponding four types of ultratransparent PhCs are of the same lattice constant *a* and of 4, 2, 2, and 1 units for the A, B, C, and D layers, respectively. The EFCs of PhCs and the discretized layers of TO media are shown in **Figure 17(c)**. It can be seen that the EFCs of PhCs have almost the same shapes with their corresponding layers, but are "shifted" by π/a in the k-space.

The detailed parameters of the PhCs are presented in **Figure 18**. The insets present the illustrations of unit cells, relative permittivities, and thicknesses of each component of the four different PhCs. Moreover, the transmittance through PhC slabs with 10 unit cells is plotted as the function of incident angles, as shown by the solid lines in **Figure 18**(**a–d**). During the calculation, the background media are chosen as the discretized TO media (**Figure 17(b)**) with the parameters $\left\{\mu_x, \mu_y, \varepsilon_z\right\}$ being $\{1.52, 0.658, 0.793\}$, $\{1.64, 0.61, 0.855\}$, $\{1.84, 0.543, 0.96\}$, and $\{2.045, 0.489, 1.067\}$, respectively. It is clearly seen that the four PhCs all have near-unity transmittance in a wide-angle range $(0 - 70^{\circ})$.

http://dx.doi.org/10.5772/intechopen.71274

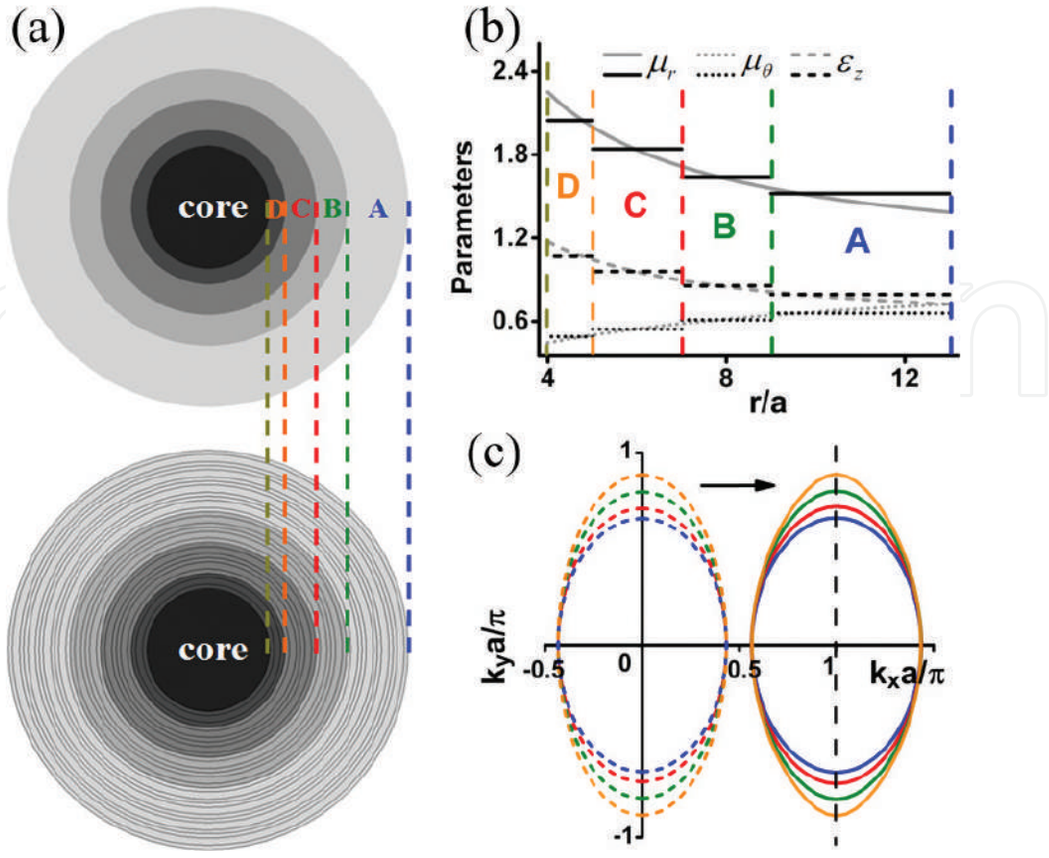

Figure 17. (a) Illustration of the design process from a concentrator composed of discretized layers of TO media (upper) to one composed of ultratransparent PhCs (lower). (b) Parameters of the discretized layers of TO media and the ideal profile. (c) EFCs of the discretized layers of TO media (dashed lines) and the corresponding PhCs (solid lines). Reprinted (figure) with permission from Ref. [21]. Copyright (2016) by the American Physical Society.

Moreover, numerical simulations are performed to demonstrate the functionality of the concentrator. **Figure 19(a)** and **(b)** corresponds to the concentrator composed of the original discretized TO media and the ultratransparent PhCs, respectively. It is seen that under an incident beam of Gaussian wave from the lower left, both concentrators exhibit good concentration effects in the core areas and induce almost no scattering of waves. Interestingly, the waves inside the core areas exhibit a distinct phase difference of π. This discrepancy is a result of the new freedom introduced by the "shift" of EFCs in the k-space, i.e., spatial dispersion.

Therefore, we have demonstrated that ultratransparent media can work as the TO media to realize TO devices. Such ultratransparent media not only provide a low-loss and feasible platform for TO devices at optical frequencies, but also enable new freedom for phase manipulation beyond the local medium framework.

5.2. For microwave transparency

In the microwave regime, the ultratransparent media are also very useful and may have many applications in the design of radome, transparent wall, and so on. Here, we show an example

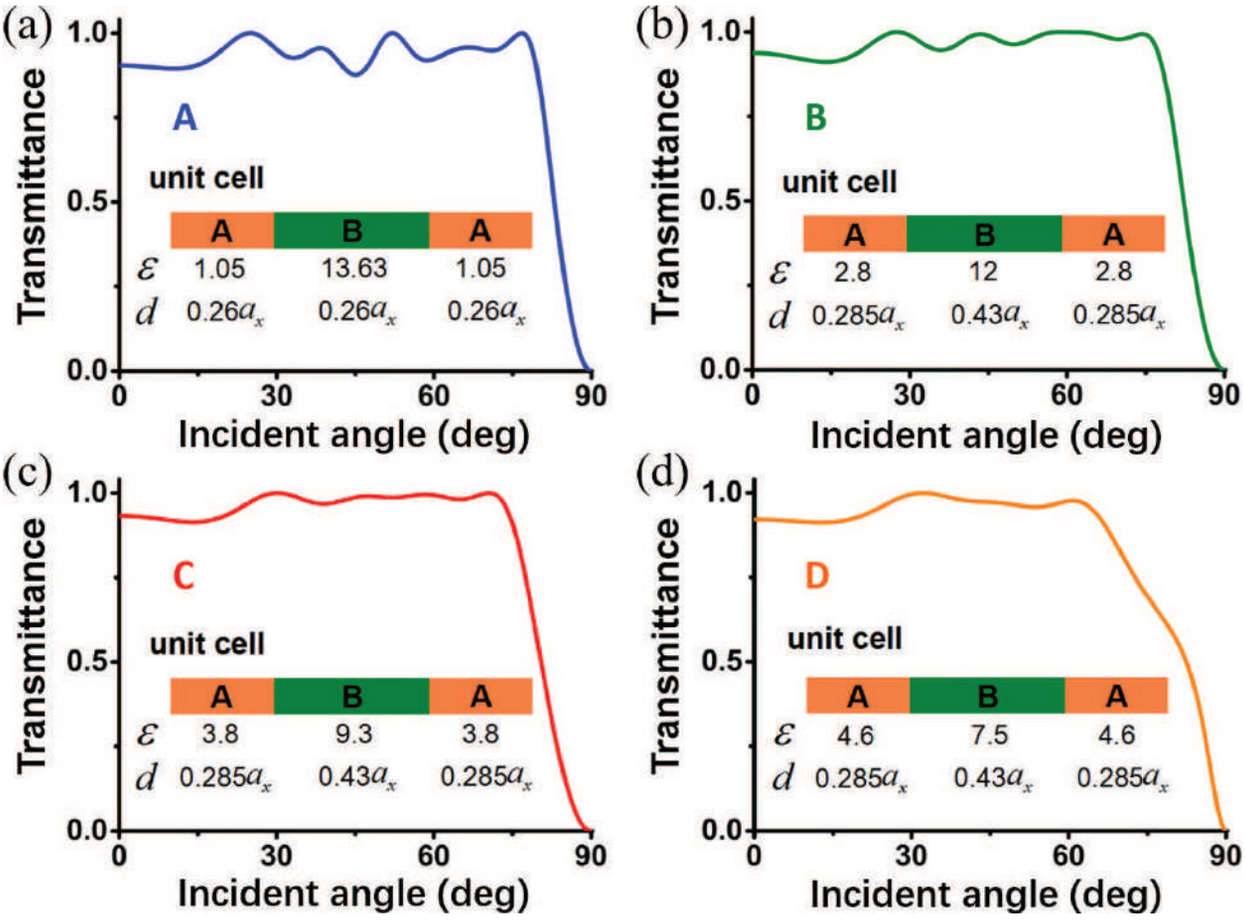

Figure 18. Transmittance through the PhC slabs with 10 unit cells as the function of incident angles. The PhCs in (a), (b), (c), and (d) correspond to the PhCs in regions A, B, C, and D, respectively. The insets are the structure, the relative permittivities, and the thicknesses of the components of the PhCs.

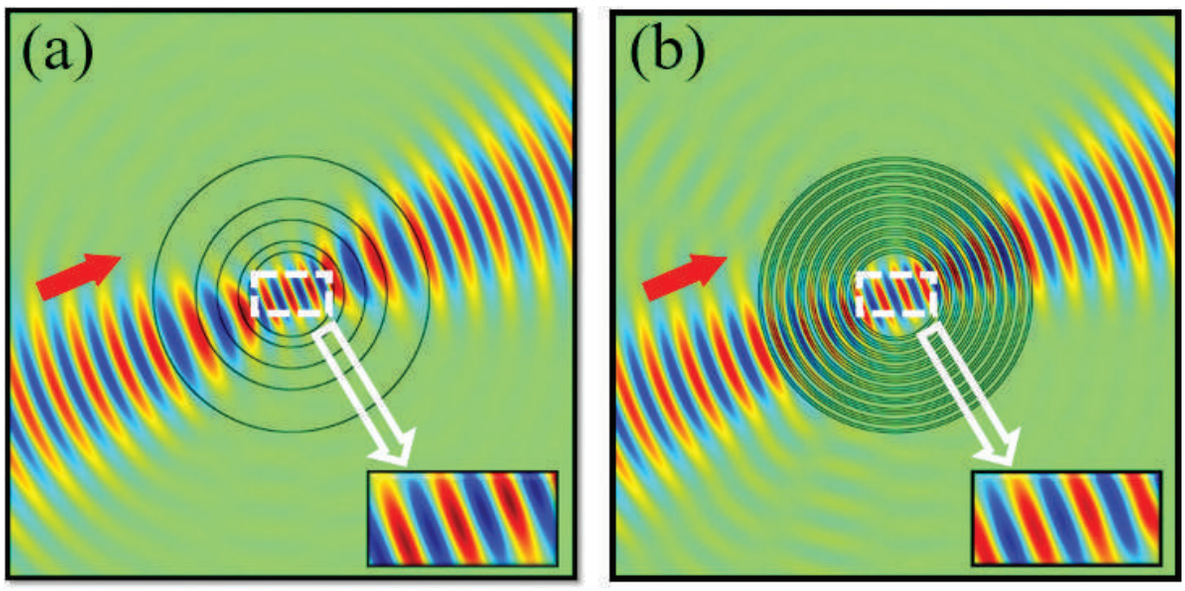

Figure 19. Electric field distributions in the concentrators made of (a) discretized TO media and (b) ultratransparent PhCs. Reprinted (figure) with permission from Ref. [21]. Copyright (2016) by the American Physical Society.

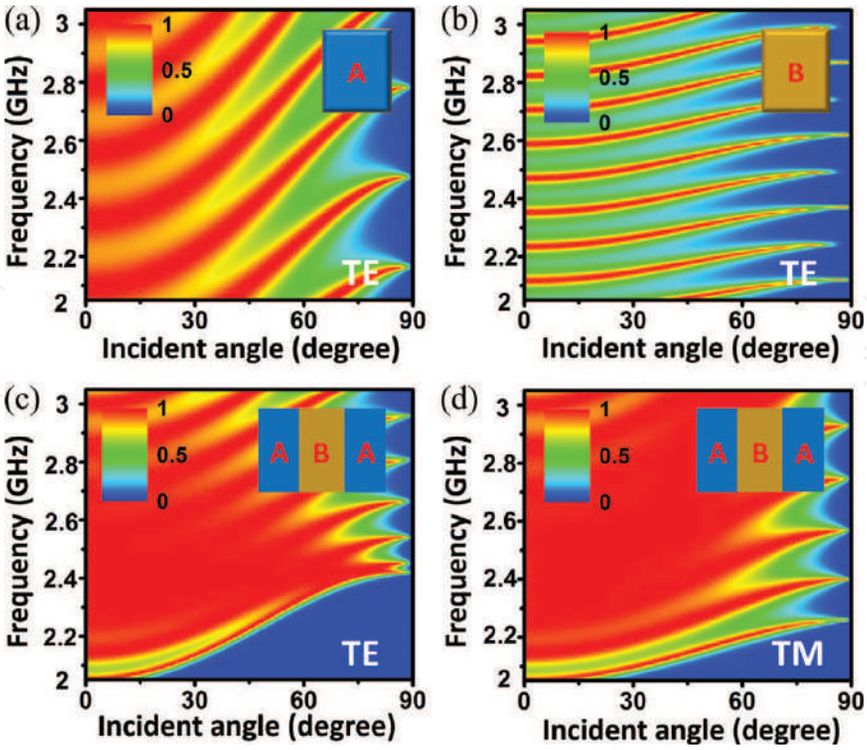

Figure 20. Transmittance with respect to the incident angle and the frequency for EM waves propagating through a slab made of (a) material A for the TE polarization, (b) material B for the TE polarization, (c, d) 10 unit cells of ABA for the (c) TE and (d) TM polarizations. Reprinted (figure) with permission from Ref. [22]. Copyright (2016) by the Optical Society.

of microwave transparent wall which allows the WiFi and 4G signals to pass through freely, and thus may find applications in architectural designs.

The microwave transparent wall is composed of one-dimensional ultratransparent PhCs with ABA unit cells. Materials A and B are chosen as polypropylene ($\varepsilon_A = 2.3$) and concrete ($\varepsilon_B = 9$). As we know, a wall (with a thickness of 42.5 cm) composed of only material A or B would lead to Fabry-Pérot resonance-induced oscillation in the transmission spectrum, as shown by the **Figure 20(a)** and **(b)**. Interestingly, if we utilize the composite structure with ABA unit cells, broadband, wide-angle, and polarization-insensitive transparency can be obtained. Specifically, the lattice constant a of the unit cell is set to be 4.25 cm, and the filling ratio of the material A (B) is 0.6 (0.4). In **Figure 20(c)** and **(d)**, the transmittance through a wall of 10 unit cells is plotted as the function of the incident angle and the working frequency for TE and TM polarizations, respectively. Obviously, almost 100% transmittance is obtained in a broad frequency band (from 2.3 GHz to 2.7 GHz) and a wide-angle range (for almost all $\theta < 60^\circ$) for both polarizations. We note that the frequency range covers the working frequency of Wi-Fi signal (with 2.4 GHz) and 4G signal (2.3 GHz~2.7 GHz). Thus, such microwave transparent walls may have applications in architectural designs.

6. Conclusions and outlook

In this chapter, we introduced the recent results of the structure-induced ultratransparency effect in both one- and two-dimensional PhCs, which allow near 100% transmission of light

for all incident angles and create aberration-free virtual images. The ultratransparency effect is well explained by nonlocal effective medium theory for PhCs and verified by both simulations and proof-of-principle microwave experiments. The design principle lies in systematic tuning of the microstructures of the PhCs based on the retrieved nonlocal effective parameters.

With the ultratransparent media, many applications can be expected such as the perfectly transparent optical lens, ideal TO devices, microwave transparent devices, and solar cell packaging. Interestingly, the ultratransparent media with "shifted" elliptical EFC not only provides a low-loss and feasible platform for TO devices at optical frequencies, but also enables new degrees of freedoms for phase manipulation beyond the local medium framework. In addition, microwave transparent walls allowing the WiFi and 4G signals to pass through freely can also be realized.

Although the ultratransparency effect is mainly demonstrated for TE polarization here, the principle is general and can be extended to TM polarization, or even both polarizations. Polarization-independent ultratransparency has wide and important applications. On the other hand, polarization-dependent ultratransparent media could also have some special applications. For instance, if the PhC is ultratransparent for TE polarization, while the working frequency falls in an omnidirectional band gap for TM polarization, such a PhC would work as an omnidirectional polarizer.

The concept and theory of ultratransparency give a guideline for pursuing solid materials with the ultimate transparency, i.e., broadband, omnidirectional, and polarization-insensitive total transparency. In the future, ultratransparent solid materials may be optimized to exhibit an unprecedented level of transparency and find vital applications in various fields.

Acknowledgements

This chapter is supported by National Natural Science Foundation of China (No. 11374224, 11574226, 11704271), Natural Science Foundation of Jiangsu Province (No. BK20170326), Natural Science Foundation for Colleges and Universities in Jiangsu Province of China (No. 17KJB140019), Jiangsu Planned Projects for Postdoctoral Research Funds (1701181B) and a Project Funded by the Priority Academic Program Development of Jiangsu Higher Education Institutions (PAPD).

Author details

Jie Luo and Yun Lai*

*Address all correspondence to: laiyun@suda.edu.cn

College of Physics, Optoelectronics and Energy and Collaborative Innovation Center of Suzhou Nano Science and Technology, Soochow University, Suzhou, China

References

[1] Yablonovitch E. Inhibited spontaneous emission in solid-state physics and electronics. Physical Review Letters. 1987;**58**:2059-2062

[2] John S. Strong localization of photons in certain disordered dielectric superlattices. Physical Review Letters. 1987;**58**:2486-2489

[3] Joannopoulos JD, Villeneuve PR, Fan S. Photonic crystals: Putting a new twist on light. Nature. 1997;**386**:143-149

[4] Joannopoulos JD, Johnson SG, Winn JN, Meade RD. Photonic Crystals: Molding the Flow of Light. 2nd ed. Princeton, USA: Princeton University Press; 2008:63-121

[5] Sakoda K. Optical Properties of Photonic Crystals. New York, USA: Springer; 2005:99-250

[6] Ho K, Chan C, Soukoulis C. Existence of a photonic gap in periodic dielectric structures. Physical Review Letters. 1990;**65**:3152-3155

[7] Fink Y, Winn JN, Fan S, Chen C, Michel J, Joannopoulos JD, Thomas EL. A dielectric omnidirectional reflector. Science. 1998;**282**:1679-1682

[8] Mekis A, Chen JC, Kurland I, Fan SH, Villeneuve PR, Joannopoulos JD. High transmission through sharp bends in photonic crystal waveguides. Physical Review Letters. 1996;**77**: 3787-3790

[9] Lin S, Chow E, Hietala V, Villeneuve PR, Joannopoulos JD. Experimental demonstration of guiding and bending of electromagnetic waves in a photonic crystal. Science. 1998;**282**: 274-276

[10] Russell P. Photonic crystal fibers. Science. 2003;**299**:358-362

[11] Painter O, Lee RK, Scherer A, Yariv A, O'Brien JD, Dapkus IKPD. Two-dimensional photonic band-gap defect mode laser. Science. 1999;**284**:1819-1821

[12] Yamamoto T, Pashkin YA, Astafiev O, Nakamura Y, Tsai JS. High-Q photonic nanocavity in a two-dimensional photonic crystal. Nature. 2003;**425**:941-944

[13] Shen Y, Ye D, Celanovic I, Johnson SG, Joannopoulos JD, Soljacic M. Optical broadband angular selectivity. Science. 2014;**343**:1499-1501

[14] Pendry JB, Holden AJ, Stewart WJ, Youngs II. Extremely low frequency plasmons in metallic mesostructures. Physical Review Letters. 1996;**76**:4773-4776

[15] Pendry JB, Holden AJ, Robbins DJ, Stewart WJ. Magnetism from conductors and enhanced nonlinear phenomena. IEEE Transactions on Microwave Theory and Techniques. 1999;**47**: 2075-2084

[16] Smith DR, Padilla WJ, Vier DC, Nemat-Nasser SC, Schultz S. Composite medium with simultaneously negative permeability and permittivity. Physical Review Letters. 2000;**84**: 4184-4187

[17] Shelby RA, Smith DR, Schultz S. Experimental verification of a negative index of refraction. Science. 2001;**292**:77-79

[18] Pendry JB. Negative refraction makes a perfect lens. Physical Review Letters. 2000;**85**: 3966-3969

[19] Zheludev NI. The road ahead for metamaterials. Science. 2010;**328**:582-583

[20] Liu Y, Zhang X. Metamaterials: A new frontier of science and technology. Chemical Society Reviews. 2011;**40**:2494-2507

[21] Luo J, Yang Y, Yao Z, Lu W, Hou B, Hang ZH, Chan CT, Lai Y. Ultratransparent media and transformation optics with shifted spatial dispersions. Physical Review Letters. 2016;**117**:223901

[22] Yao Z, Luo J, Lai Y. Photonic crystals with broadband, wide-angle, and polarization-insensitive transparency. Optics Letters. 2016;**41**:5106-5109

[23] Pendry JB, Schurig D, Smith DR. Controlling electromagnetic fields. Science. 2006;**312**: 1780-1782

[24] Leonhardt U. Optical conformal mapping. Science. 2006;**312**:1777-1780

[25] Schurig D, Mock JJ, Justice BJ, Cummer SA, Pendry JB, Starr AF, Smith DR. Metamaterial electromagnetic cloak at microwave frequencies. Science. 2006;**314**:977-980

[26] Chen H, Chan CT, Sheng P. Transformation optics and metamaterials. Nature Materials. 2010;**9**:387-396

[27] Pendry JB, Aubry A, Smith DR, Maier SA. Transformation optics and subwavelength control of light. Science. 2012;**337**:549-552

[28] Śmigaj W, Gralak B. Validity of the effective-medium approximation of photonic crystals. Physical Review B. 2008;**77**:235445

[29] Lu Z, Prather DW. Calculation of effective permittivity, permeability, and surface impedance of negative-refraction photonic crystals. Optics Express. 2007;**15**:8340-8345

[30] Lawrence FJ, de Sterke CM, Botten LC, McPhedran RC, Dossou KB. Modeling photonic crystal interfaces and stacks: Impedance-based approaches. Advances in Optics and Photonics. 2013;**5**:385

[31] Li J, Pendry JB. Hiding under the carpet: A new strategy for cloaking. Physical Review Letters. 2008;**101**:203901

[32] Lai Y, Chen H, Zhang Z, Chan C. Complementary media invisibility cloak that cloaks objects at a distance outside the cloaking shell. Physical Review Letters. 2009;**102**:093901

[33] Rahm M, Schurig D, Roberts DA, Cummer SA, Smith DR, Pendry JB. Design of electromagnetic cloaks and concentrators using form-invariant coordinate transformations of Maxwell's equations. Photonics and Nanostructures. 2008;**6**:87-95

[34] Lai Y, Ng J, Chen H, Han D, Xiao J, Zhang Z, Chan C. Illusion optics: The optical transformation of an object into another object. Physical Review Letters. 2009;**102**:253902

[35] Pendry J. All smoke and metamaterials. Nature. 2009;**460**:79-580

[36] Lai Y, Ng J, Chen H, Zhang Z, Chan CT. Illusion optics. Frontiers of Physics China. 2010;**5**:308-318

[37] Genov DA, Zhang S, Zhang X. Mimicking celestial mechanics in metamaterials. Nature Physics. 2009;**5**:687-692

[38] Sheng C, Liu H, Wang Y, Zhu SN, Genov DA. Trapping light by mimicking gravitational lensing. Nature Photonics. 2013;**7**:902-906

[39] Cai W, Chettiar UK, Kildishev AV, Shalaev VM. Optical cloaking with metamaterials. Nature Photonics. 2007;**1**:224-227

[40] Liu R, Ji C, Mock JJ, Chin JY, Cui TJ, Smith DR. Broadband ground-plane cloak. Science. 2009;**323**:366-369

[41] Valentine J, Li J, Zentgraf T, Bartal G, Zhang X. An optical cloak made of dielectrics. Nature Materials. 2009;**8**:568-571

[42] Gabrielli LH, Cardenas J, Poitras CB, Lipson M. Silicon nanostructure cloak operating at optical frequencies. Nature Photonics. 2009;**3**:461-463

[43] Ergin T, Stenger N, Brenner P, Pendry JB, Wegener M. Three-dimensional invisibility cloak at optical wavelengths. Science. 2010;**328**:337-339

[44] Ma HF, Cui TJ. Three-dimensional broadband ground-plane cloak made of metamaterials. Nature Communications. 2010;**1**:21

[45] Xu S, Cheng X, Xi S, Zhang R, Moser HO, Shen Z, Xu Y, Huang Z, Zhang X, Yu F, Zhang B, Chen H. Experimental demonstration of a free-space cylindrical cloak without superluminal propagation. Physical Review Letters. 2012;**109**:223903

[46] Xiao S, Drachev VP, Kildishev AV, Ni X, Chettiar UK, Yuan HK, Shalaev VM. Loss-free and active optical negative-index metamaterials. Nature. 2010;**466**:735-738

[47] Hess O, Pendry JB, Maier SA, Oulton RF, Hamm JM, Tsakmakidis KL. Active nanoplasmonic metamaterials. Nature Materials. 2012;**11**:573-584

[48] Lai Y, Zheng H, Zhang Z, Chan CT. Manipulating sources using transformation optics with 'folded geometry'. Journal of Optics. 2011;**13**:024009

IntechOpen

Chapter 5

Influence of Substrate Wettability on Colloidal Assembly

Junchao Liu, Jingxia Wang and Lei Jiang

Additional information is available at the end of the chapter

http://dx.doi.org/10.5772/intechopen.71991

Abstract

In this paper, we presented a detailed discussion about the influence of the substrate wettability on the colloidal assembly and the resultant functionality of the films. It covers the basic assembly principle for colloidal crystals, the basic understanding of the substrate wettability on colloidal assembly, and the detailed explanation of the influence by give a full examples of various assembly from the substrate with distinct wettability, such as superhydrophilic, hydrophilic, hydrophobic, superhydrophobic and hydrophilic-hydrophobic pattern substrate.

Keywords: wettability of substrate, colloidal crystals, assembly

1. Introduction

Colloidal crystals [1–4] has aroused wide research attention owing to its fascinating light manipulation properties and important application in sensing [5–18], detecting [19–22], catalytic [23, 24] and some special optic devices [25–32]. Colloidal crystals are generally fabricated from the well-ordered assembly of the monodispersed latex particles or infiltrating the functional materials into the template and subsequent template removal (the typical fabrication process for the inverse opals). Accordingly, colloidal assembly plays an important role on the resultant functional, unique properties and the resulted potential applications. In this paper, we presented a detailed discussion about the influence of the substrate wettability on the colloidal assembly and the resultant functionality of the films. It covers the basic assembly principle for colloidal crystals, the basic understanding of the substrate wettability on colloidal assembly, and the detailed explanation of the influence by giving a full examples of various assembly from the substrate with distinct wettability, such as superhydrophilic, hydrophilic, hydrophobic, superhydrophobic and hydrophilic-hydrophobic pattern substrate.

2. Basic assembly principle for colloidal crystals

Colloidal assembly has become a well-known process since more than 5 decades' investigation of the colloidal assembly [33]. As shown in **Figure 1**, the colloidal assembly process includes the crystal nucleus by capillary force among latex particles, when the liquid front covers the half of the particles and crystal growth driven by the convective force owing to solvent evaporation and solvent reflux. A common mode for colloidal assembly includes vertical deposition approach. Where, the substrate is vertically placed in a colloidal solution, then a film of colloidal particles is formed at the interface between the substrate and the liquid surface with the solvent evaporation and the liquid surface drops. The formation of colloidal assembly is mainly originated from the driven force of capillary force between the drying colloidal particles at the meniscus of the solvent [34].

It is well known that the colloidal assembly is mainly depended on the assembly temperature, assembly humidity, and plenty of researches literatures took a careful investigation of the influence of various influencing factors on assembly behavior, assembly structure, and resultant property of colloidal crystals. Meantime, many assembly approach, such as spin coating, spray coating, inkjet printing, has been developed to improve the duplicated, assembly rate, controllable assembly, scalable assembly and high-quality assembly. Where, the vertical deposition approach has become a common method owing to its economic and easily duplicated in most laboratory (**Figure 1C**). In this following part, we would like to discuss the influence of the substrate wettability on colloidal assembly.

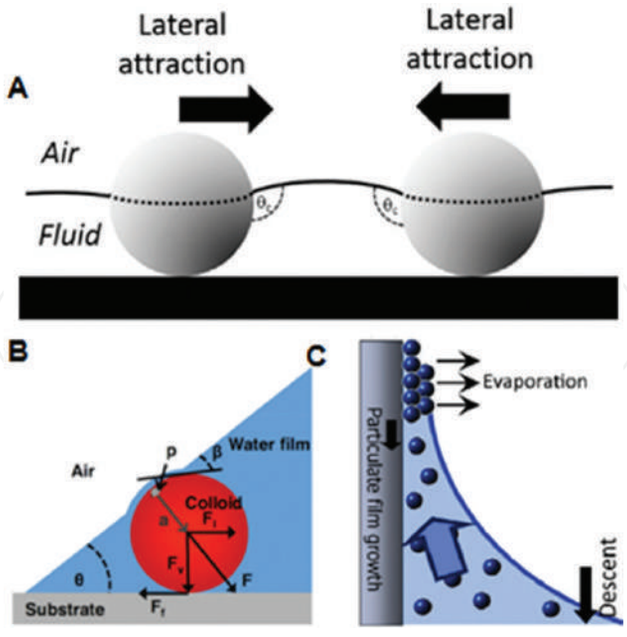

Figure 1. Mechanism of colloidal PCs assembly. (A) Colloidal particles assembly forced by the liquid flow as evaporation of the solvent; (B) acting on a colloid trapped at an air water substrate interface; (C) schematic illustration of the convective self-assembly technique in vertical deposition way [33, 34].

http://dx.doi.org/10.5772/intechopen.71991

3. Basic understanding of the substrate's wettability on colloidal assembly

To understand the basic influence of the wettability on colloidal assembly, we present a basic concept of the substrate wettability and depict a detailed analysis about the effect of substrate wettability on the assembly process, assembly force and etc.

3.1. Basic concept of substrate wettability and the basic understanding of the wettability on the colloidal assembly

Wettability is a basic property of liquid on solid surface, it is determined by surface chemical composition and surface roughness, as shown in **Figure 2**. Generally, the wettability is evaluated by the water contact angle (CA), i.e., static CA. It is defined by integrated angle for the three-phase contact line of liquid, gas and solid after a droplet spread on the substrate (**Figure 2A**). Based on different statistic CA, distinct substrate is determined. The hydrophilic substrate with CA < 65°, indicating a strong attraction of liquid on solid surface, which results in droplet spreading. Especially superhydrophilic substrate is obtained when CA is around 0° (**Figure 2C**). Hydrophobic substrate with CA > 90°, meaning a limited attraction between solid and liquid surface, a less spread is observed for droplet on the substrate. Recently, the diving line is set as 65°, a new dividing line

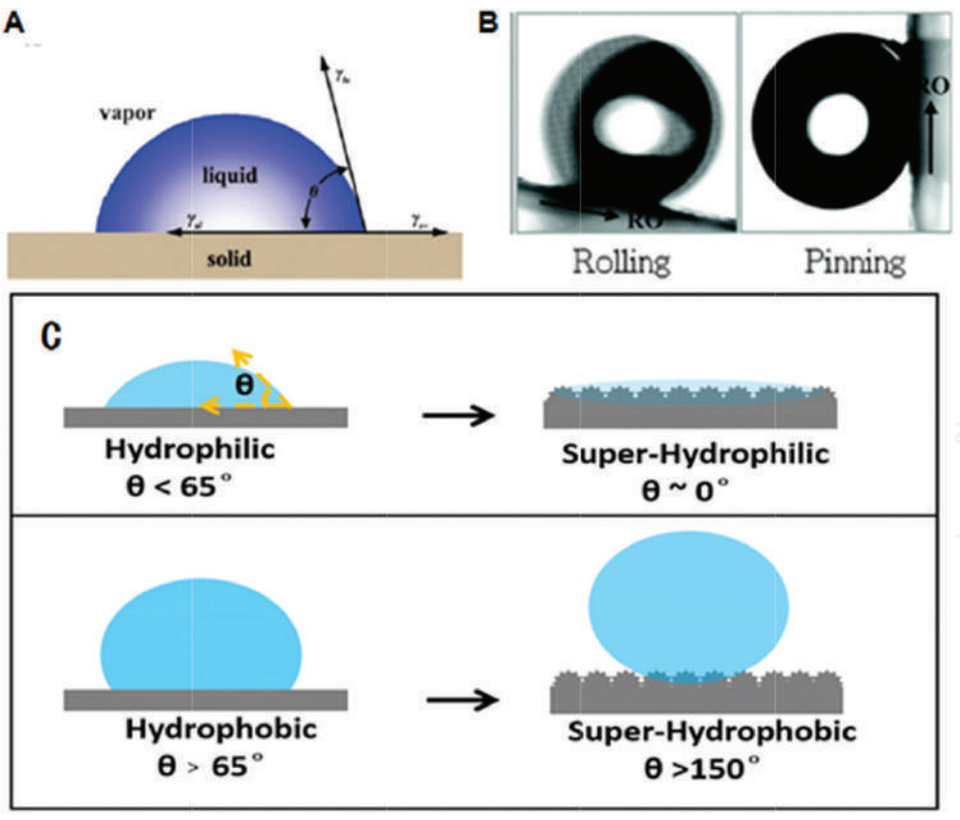

Figure 2. Wettability of interfaces. (A) Statistic contact angle, (B) sliding angle with different substrate adhesive, (C) schematic illustration of different wettability state [35].

between hydrophilic and hydrophobic, is defined by Prof. Lei Jiang. Superhydrophobic substrate with water CA > 150°, is a special substrate, it is difficult for the droplet to spread upon it. Such as the lotus surface. Besides statistic CA, sliding angle is also a judgment of wettability of substrate. As shown in **Figure 2B**, when a droplet and three phase contact line (TCL) can stay steadily on a solid substrate it indicates high-adhesive, in the contrast, droplet and TCL can easily move on a low-adhesive substrate. Both static CA and the sliding angle plays an important role on the colloidal assembly. The substrate with different water CA showed various potential applications.

3.2. Basic understanding of the influence of the substrate wettability on colloidal assembly from static and dynamic wettability

Here, we understand the influence of the substrate's wettability on colloidal assembly by qualitatively analyzing the relationship between the substrate wettability on the evaporation time/rate and the evaporation force when a droplet spreading on the substrate. As shown in **Figure 3**, for the hydrophilic substrate with lower CA, having a large spreading area. In this

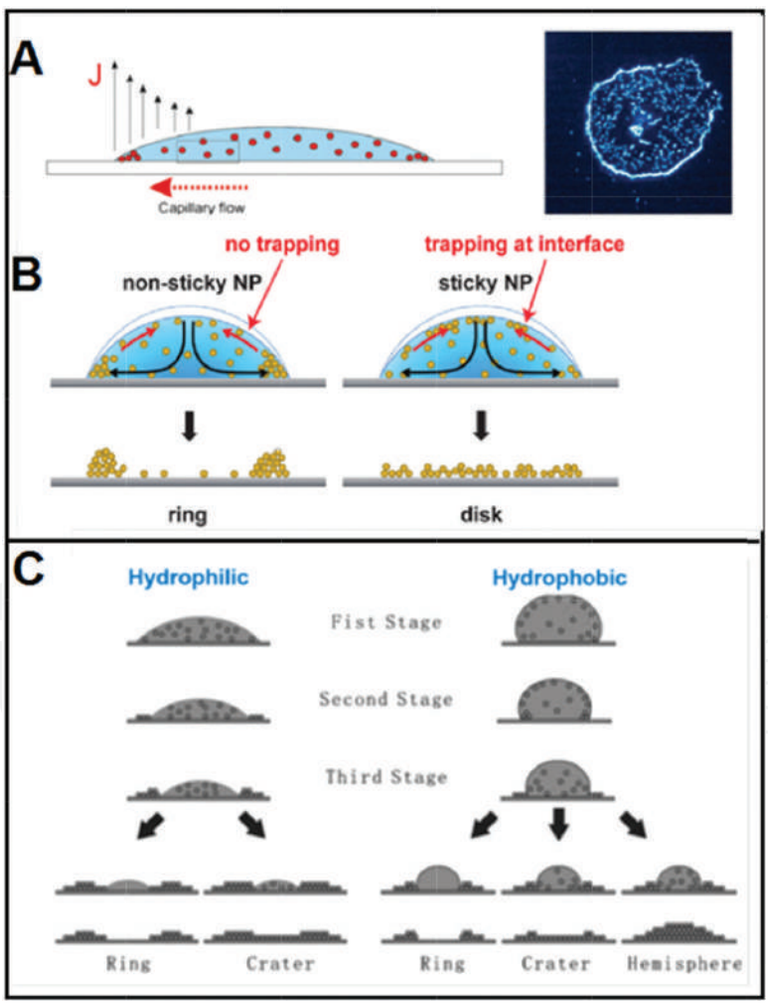

Figure 3. Formation of colloidal PCs as substrate is hydrophilic. (A) Illustration of coffee stain formation and a microscope image of a coffee stain formed by fluorescently labeled 5-μm particles; (B) on a hydrophilic substrate, the competition of Marangoni flow (red arrows) and the evaporation-driven capillary flow (black arrows) resulted the ring-shape or the disk shape. (C) Schematic depiction of the aggregation of monodisperse spheres on hydrophilic PMMA and hydrophobic FAS-coated glass substrates [36].

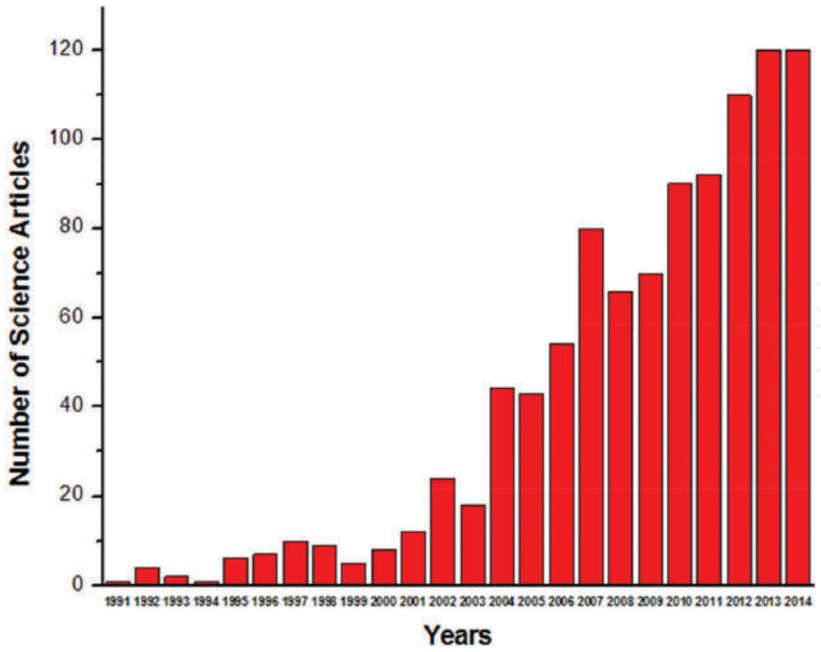

Figure 4. Number of science articles that searching result of "assembly" + "wettability".

case, the droplet keeps constant contact area and decreased water CA during evaporation process, as a result, a short time or fast evaporation rate is observed for the droplet evaporation. In contrast, when droplet is on the hydrophobic substrate, the droplet keeps constant CA but a decreased contact area during evaporation process. As a result, a longer evaporation time and slower evaporation rate occurs in the evaporation system. Accordingly, there would be a short assembly time on hydrophilic substrate, and a longer assembly time on hydrophobic substrate. On the other hand, substrate wettability will affects the pinning or sliding or TCL on the substrate, the sliding TCL will produce an addition driven force for the latex assembly, will contributing to distinct assembly structure and colloidal property as well.

As regarding of the research progress related to the influence of the wettability on colloidal assembly, there is an obvious increased paper published after Year 2004, as shown in **Figure 4**. Which presented the research papers number (related to colloidal assembly & wettability) ranging from 1991 to 2014, the data is searched from database of Web of Science. Clearly, less papers is related to the colloidal assembly &wettability prior to 2004, there are only 1–2 papers published in 1991. In comparison, a rapid growth of the paper numbers related to colloidal assembly/wettability occurred after the period. More than 100 papers published related to the topic in Year 2014. In the following part, we will list a full example to understand what the influence of the substrate's wettability on the colloidal assembly.

4. Full examples for the understanding of the influence of wettability on colloidal assembly

Wettability of substrate plays an important effect on the colloidal assembly by affecting its assembly time, assembly rate and assembly process. In this section, we summarized various

examples to give a full description of the influence of the wettability on the colloidal assembly process and its resultant assembly structure. Wherein, the substrate with wettability, such as superhydrophilic, hydrophilic, hydrophobic, superhydrophobic, pattern-substrate is considered.

4.1. Superhydrophilic substrate

Superhydrophilic substrate with water CA of 0°, shows excellent spreading behavior for the colloidal suspension. In this case, the resultant colloidal assembly structure showed an uniform distribution. Therefore, superhydrophilic substrate is generally thought to be optimal substrate for the colloidal assembly at the earlier assembly literature. How to achieve a superhydrophilic substrate has ever to be an important technical issue for the well-ordered colloidal assembly [37]. Accordingly, many early assembled literatures are carried out on superhydrophilic substrate. Many outstanding and impressing assembly work is done on superhydrophilic substrate. Typically, many colloidal crystals are assembled on superhydrophilic substrate by vertical deposition, spin coating, spray coating.

4.2. Hydrophilic substrate

Hydrophilic substrate with water CA <65° have a special "coffee-ring" effect on colloidal assembly. Coffee ring is aroused owing to the faster evaporation rate in the exterior region of the droplet comparing that interior region, thus more latex transfer from the interior toward the exterior region, which resulted in the more deposit and assembly of the latex particles at the brim of the droplet, leaving less latex at the center of the droplet, forming a ring-shaped structure (left part of **Figure 3B** and **C**). Much work is developed to remove coffee ring effect by introducing temperature filed, surfactant. Of course, some researchers fabricated some interesting pattern by taking advantage of the coffee-ring effect. For example, Gu et al. [36] displayed different assemble modes of PC in hydrophilic and hydrophobic substrate in **Figure 3**. They used different concentration suspension dripple onto polymethyl methacrylate (PMMA) substrate and FAS-treated glass substrate in the hydrophilic substrate, ring and crater structure can be obtained, while on hydrophobic substrate, hemisphere structure also appear for the liquid shrink to a dot. The assembly process of colloidal particles on different wettability substrate can be described as follows. Furthermore, Gu et al. developed a ring-shape colloidal crystal by taking advantage of coffee-ring phenomenon for artificial eye-pupil structure.

4.3. Hydrophobic substrate

Hydrophobic substrate with water CA of higher than 65°, showed special evaporation behavior than that on the hydrophilic substrate. Particularly, TCL recedes owing to the lower adhesive force of particles on the substrate when droplet evaporating on hydrophobic substrate. Just because the receding TCL, the coffee ring effect can be effectively removed on hydrophobic substrate (right part in **Figure 3B** and **C**). In this case, a sphere-rich phase near the solvent/air interface was caused by evaporation of the solvent (first stage); the crystallization of spheres at the rim of drop occurred when the concentration exceeded a critical value (second

stage); receding TCL aggregate the latex toward the center of the droplet (third stage). As a result, a final compact assembly structure can be obtained "similar to dome". The application of the hydrophobic substrate may produce some novel and functional assembly structure.

Liu et al. [38] fabricated controllable inkjet printing lines by adjusting the ink droplets' dynamic wettability on hydrophobic substrate (**Figure 5A** and **B**). Mixing the ink with water and ethylene glycol to adjust the ink droplet's surface tension and the nanoparticle concentration. Distinct dynamic wettability of ink droplets on the hydrophobic substrate could be achieved owing to the different surface tension and nanoparticle concentration. In the first case, the surface tension of droplet 1 and 2 were similar, the TCL of droplet was hardly pinned owing to no particle assembly at TCL. A spherical cap was obtained after coalescing and drying of ink, as shown in **Figure 5A**$_1$. In contrast, if the surface tension of droplet 1 was smaller than droplet 2, the TCL of droplet was pinned and a straight line could be obtained after coalescing and drying owing to nanoparticles assembled at the TCL of the droplet 1. Furthermore, a stronger pinning TCL and dumbbell shape was formed with more nanoparticles assembling at the TCL, as shown in **Figure 5A**$_2$ and **A**$_3$. As a result, different line shapes of wave, straight footprint and wave with straight footprint were obtained, as shown in **Figure 5B**. Hydrophobic substrate was used for the removal of the coffee ring. Typically, Cui et al. [40] made a research about a drop of a colloidal suspension of latex spheres dropped onto a hydrophobic-silica pillar array (HSPA) with high contact hysteresis to remove coffee ring effect. In details, a drop of colloidal suspension with latex spheres presents a Wenzel state with high CA hysteresis on the surface of HSPA, which leads to the pinning of contact line (CL) during the solvent evaporation. Then more latex spheres will be deposited on the periphery of the drop to accelerate growth of the porous gel foot (means the aggregation of latex spheres at the edge of the droplet). Subsequently, the capillary

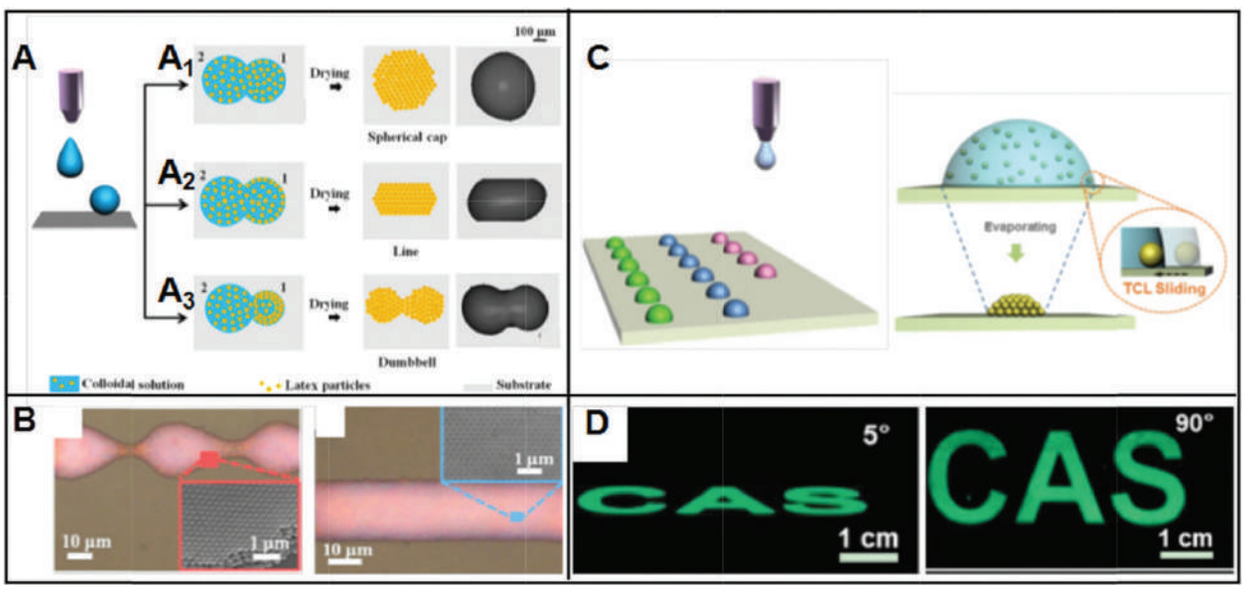

Figure 5. (A) Three typical coalescing cases of the neighboring ink droplets induced by different dynamic wettability of ink droplets on the substrates. (B) Optical microscope images of the as-printed PC lines with wave and straight footprints. Three typical straight PC lines (red, green, and blue) demonstrating good optical properties and the insets are the corresponding SEM images [38]. (C, D) fabrication of photonic crystal dome on hydrophobic substrate by inkjet printing [39].

flow formed based on a growing gel foot. Finally, a uniform colloidal deposition without a coffee ring structure is obtained owing to the existence of gel foot and capillary flow. Finally, "coffee ring" diminished as well as closed-packing PC structure can be obtained. Due to the fast shrinking of the TPCL. Furthermore, hydrophobic substrate was used for the fabricated of the PC dome array by inkjet printing by Kuang et al. [39] in **Figure 5C–D**. They inkjet printed latex suspension on the hydrophobic substrate, obtained dome-like PC sphere, which can effectively avoid the angle-dependent property of the stopband of PC, providing an important insight for the wide-view display applications of PCs. That is, the hydrophobic substrate provides an effective approach for the fabrication of colloidal crystals with excellent wide-angle property [41–46].

4.4. Superhydrophobic substrate

Superhydrophobic substrate is a special substrate with water CA > 150°, the rolling angle less than 5°, as well as low adhesive surface. The large water CA makes it possible for the spherical colloidal assembly. While the low-adhesive property of substrate contributed to the formation of crack-free colloidal assembly.

The application of superhydrophobic substrate is helpful for the fabrication of spherical PCs and crack-free colloidal PCs. For example, Velev et al. [47] reported an approach for colloidal assembly in droplets on superhydrophobic substrates (**Figure 6A**), which yields

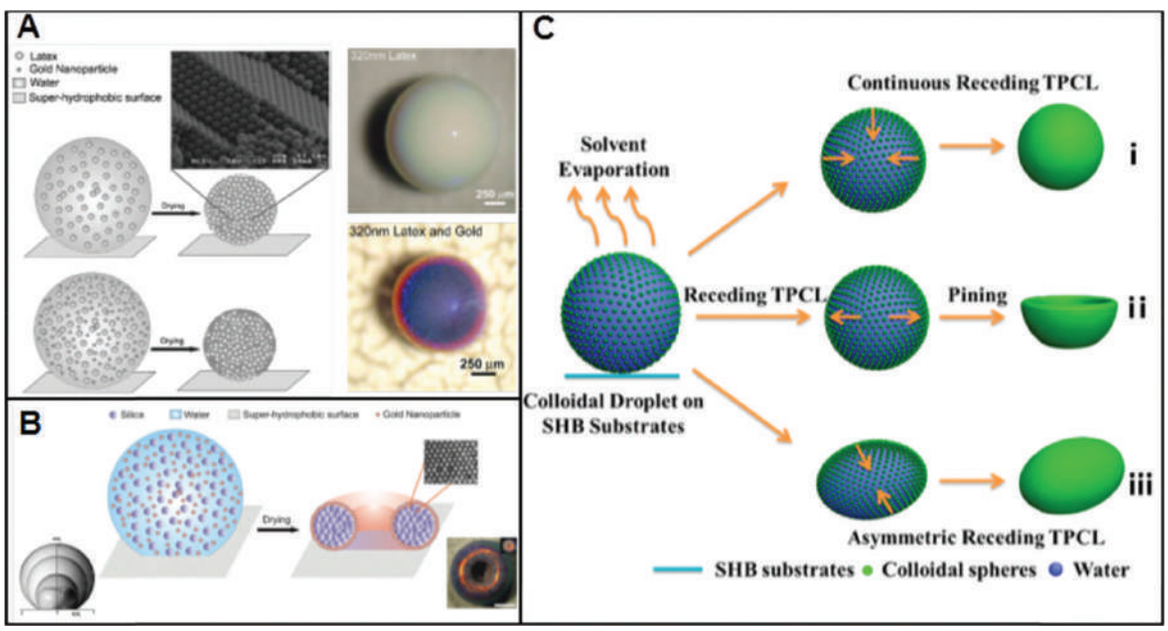

Figure 6. (A) Schematics of the process for making spherical colloidal assemblies on superhydrophobic. The inset displays the hexagonal close-packed structure of latex spheres inside an opal ball of 540 nm latex [47]. (B) Schematic of supra-particle formation by evaporating a droplet containing suspension of silica and gold nanoparticles. Top and angled view of "golden doughnut" supra-particles on the right-down inset. The inset on the left-down shows an overlay of experimental images for the side-view profile of a drying droplet with silica particles over time fabricated from a droplet containing 330-nm-diameter silica [48]. (C) Schematic illustrations of the microshape fabrication of PC particles on superhydrophobic substrates based on different dynamic behaviors of the TCL, (i) continuous receding, (ii) receding and then pinning, and (iii) asymmetric receding of the TCL [49].

better control over the final shape and creates supra-particles that are easily detached and ready to use. The resultant colloidal assembly is near-spherical and spheroidal supraballs. The process of sample are as follows: the droplet of colloidal latex or mixed with gold nanoparticles showed superhydrophobic and high CA hysteresis owing to the small pinning areas formed between low-density polyethylene and substrate. Thus the colloidal spheres were inclined to form a close-packed microsphere crystals with the evaporation of solvents due to the decrease of free volume between latex particles. As a result, the spherical colloidal PC with colored ringlike diffraction patterns was formed. Later, they developed this method and obtained shape-anisotropic ("doughnut") and composition-anisotropic ("patchy magnetic") supra-particles [48] in **Figure 6B**. At the initial stage, near-spherical shape was obtained due to a high contact angle. During the process of solvent evaporation, silica suspension droplets undergo shape transitions (concaving) leading the structure of the final assemblies to doughnut supra-particles. Furthermore, composition anisotropy is achieved by drying a droplet containing a mixed suspension of latex and magnetic nanoparticles among a magnetic field gradients. The magnetic nanoparticles assembled into single, bilateral, or trilateral, patched spherical supra-particles. Additionally, the shape of the microsphere can be tuned by Zhou et al. from microbeads to microwells to microellipsoids via adjusting the dynamic behaviors of the three-phase contact line (TCL) during the evaporating process on superhydrophobic substrates [49] (**Figure 6C**). The assembly of PC structure is prepared by dispensing aqueous colloidal latex spheres droplet (acting as self-assembly template) onto superhydrophobic substrate and evaporates naturally. The high CA (≈151°) of colloidal latex droplet on the superhydrophobic substrate contributed to the formation of self-assemblies templates. Microbead PC assemblies was obtained by continuous homogeneous receding of the TCL of the aqueous colloidal droplet evaporating on superhydrophobic substrate (scheme C_i). But for dimpled microbead or microwell PC assemblies (scheme C_{ii}), the reason for its formation maybe the change in the moving directions of the colloidal spheres caused by pinning of the TCL during aqueous colloidal droplet evaporation. Furthermore, asymmetric receding of TCL benefits the interesting anisotropic PC assemblies (scheme C_{iii}). It worth to be noted that high-quality crack-free colloidal PC can be fabricated from superhydrophobic substrate. For instance, Huang et al. [50] fabricated a centimeter scale PCs on low-adhesive super-hydrophobic substrates (**Figure 7**). It shows the schematic illustration of colloidal PCs assembled on high F_{ad} substrate and low F_{ad} superhydrophobic substrate. The red dashed lines indicate the changing trend of the TCL during different drying conditions. The latex particles at first assemble on the surface of the suspension, and then shrink with further solvent evaporation. When the latex particles dry on a substrate with high F_{ad}, the pinned TCL and latex shrinkage causes tensile stress and crack formation. In contrast, large-scale crack-free colloidal PCs are achieved on a superhydrophobic substrate with low F_{ad} due to the timely release of tensile stress as the TCL recedes. The sample showed high quality and crack-free property, it is especially important, the sample showed an evident narrow stopband with full-width-at-half-maxima of the stopbands of just 12 nm due to the receding TCL during evaporation process, which releases the tensile stress induced by latex shrinkage. The work is of great significance for the creation of novel and high-quality PC optic devices.

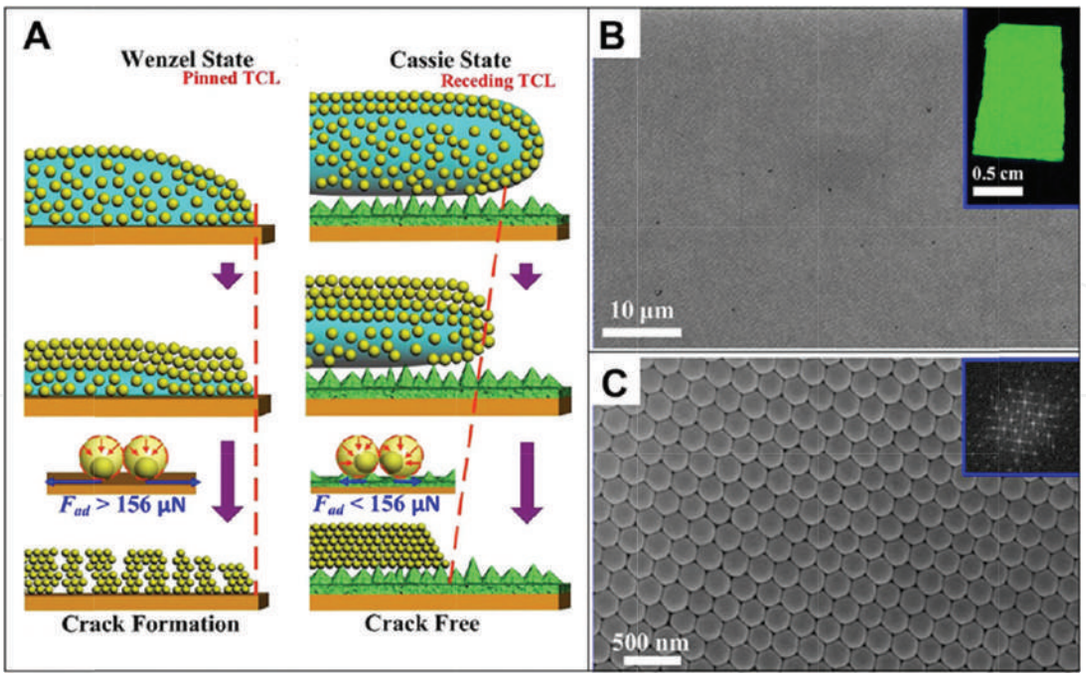

Figure 7. (A) Schematic illustration for the fabrication of crack-free PC on low-adhesive superhydrophobic substrate. (B, C) SEM images of the as-prepared colloidal PCs with diameter of 224 nm assembled on low-adhesive superhydrophobic substrate. The images demonstrate perfectly ordered latex arrangement and close-packed assembly structures of the PCs [50].

4.5. Pattern colloidal crystals from the combination of the hydrophilic/hydrophobic substrate

Wettability also can be used for design patterned PCs [51]. Colloidal crystals with different patterns in various colors may be obtained through tuning the wettability of assemble substrate, and different particles, Also, asymmetric or dissymmetric pattern can also be created in wettability gradient surface.

Figure 8A exhibited a detailed description about the fabrication of the substrate with modified wettability. For example, Young et al. demonstrated the structure of the PS colloidal crystals which were fabricated on the hydrophilic/hydrophobic Si wafers by a spin-coating technique (**Figure 8A)**. PS spheres organized as ordered close-packed face-centered cubic structure on the hydrophilic surface while they gathered without the crystal structure on the hydrophobic surface. Lee et al. [52] made site-selective assembly available and designed a surface with alternating wetting region and dewetting region in **Figure 8B**, then the particles only confined and assembled in the wet region. Therefore, wettability induced PC pattern can be obtained. The basic concept of site-selective assembly of colloidal particles on a wettability-patterned surface are shown in **Figure 8B**. The relative fraction of the wet region W to the dewet region D and droplet volume decided the wetting layer morphology including the CA. First, a generate patterned wettability was obtained by liquid crystal (LC) alignment layer irradiated via UV light through a photomask. Then a periodic array of circular W regions surrounded by intact D regions was obtained. When dropping an LC/prepolymer solution with colloidal particles on the as-prepared wettability patterned substrate, it could

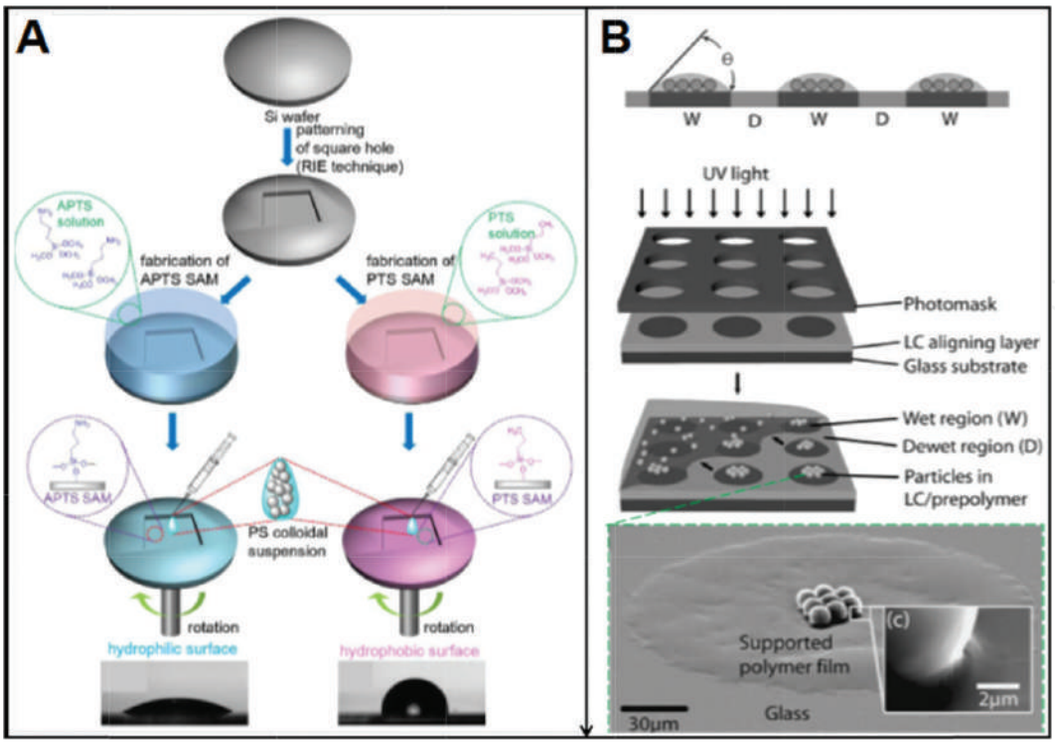

Figure 8. (A) a detailed description about the fabrication of the substrate with modified wettability. (B) schematic diagrams showing underlying concept of site-selective assembly of colloidal particles: Liquid crystal (LC)/prepolymer solution containing colloidal particles on wettability-patterned surface with wet regions (W) and dewet regions (D) and wettability-patterning process using UV exposure on LC alignment layer (top) and array of LC/prepolymer droplets produced only in wet regions where the colloidal particles are confined (bottom) [52].

be confined to the W regions. A highly close-packed structure of colloidal particles located in the W region was formed. Trough different value of H, two assembly cases of colloidal particles that in central or boundary regions could be formed.

Wu et al. [53] presented a strategy to fabricate controllable 3D structures and morphologies from one single droplet via inkjet printing (**Figure 9A** and **B**). The 3D morphology of microcolloidal crystal pattern was controlled by hydrophilic pattern induced asymmetric dewetting. First, using a hydrophobic silicon wafer with patterned hydrophilic pinning spots (green shading) as substrate. Then nanoparticles contained precisely designed droplets array was prepared by inkjet printing. Arrayed 3D microcolloidal crystals with controllable morphology were achieved owing to the hydrophilic pattern induced asymmetric dewetting. Many morphologies of quadrilateral, pentagon, hexagon and etc. could be obtained through different hydrophilic patterns. Wang et al. [54] fabricated a microring PC made of colloidal particles by taking advantage of a superhydrophilic flat transfer substrate and a superhydrophobic groove–structured silicon template (**Figure 9C**). The process of "sandwich assembly" was mainly used by a superhydrophobic groove structured template and a flat superhydrophilic transfer substrate. The as-prepared microrings showed homogeneous bring–green color owing to the fluorescent signal and favorable waveguide property. Yoo et al. [55] reported a flexible superhydrophobic PDMS cage formed by superhydrophobic patterns encompassing the unmodified region for aqueous

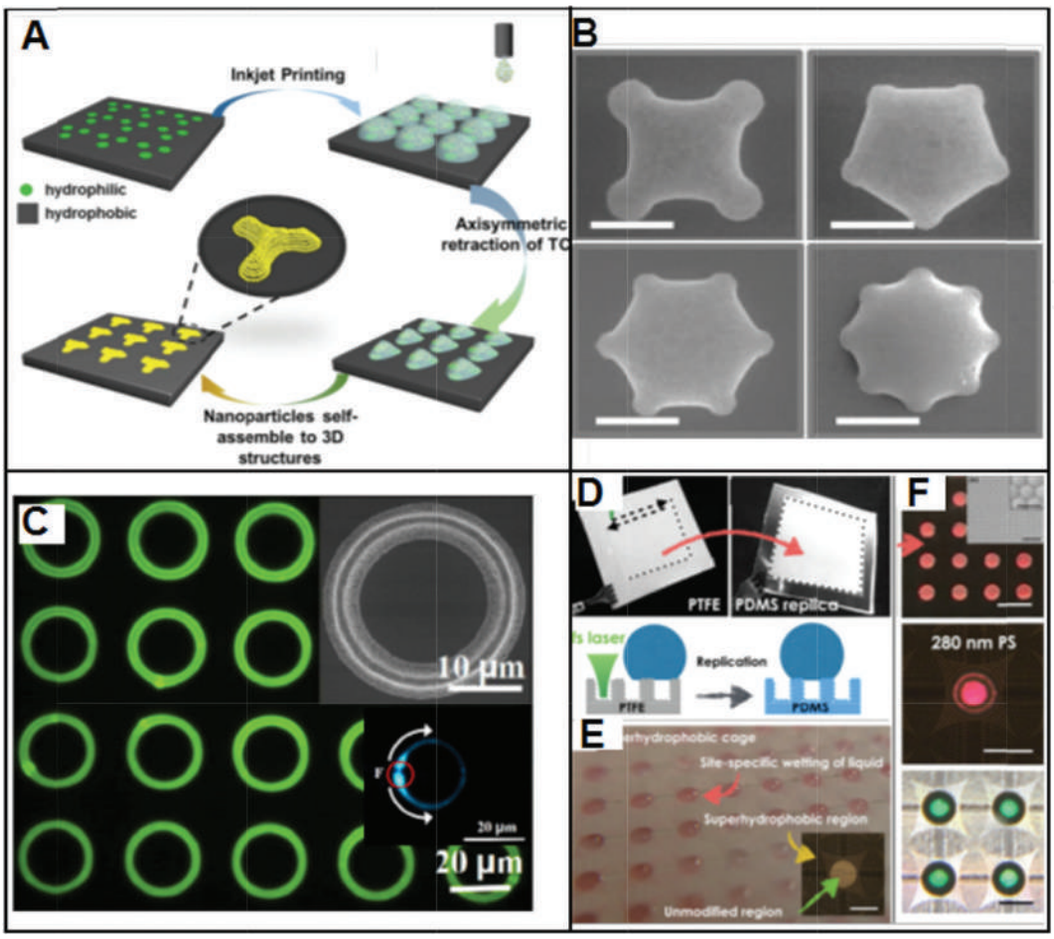

Figure 9. (A) Manipulating 3D morphology of microcolloidal crystal pattern through hydrophilic pattern induced asymmetric dewetting. (B) SEM images of various assembly units through designed hydrophilic pinning pattern [53]. (C) Fluorescence optical and SEM images of micro-ring PC and its waveguide property [54]. (D) Schematics of superhydrophobic surface production by FS laser direct writing. Photographs of superhydrophobic polytetrafluoroethylene (PTFE) film and superhydrophobic polydimethylsiloxane (PDMS) replica. (E) PDMS superhydrophobic cage. (F) Microscopic pictures of self-assembled structures on a superhydrophobic cage. The scale bars are 1 mm. Magnified reflection and transmission microscopic pictures of self-assembled structures consisting of 280 nm PS particles from colloidal droplets. Scale bars are 500 μm [55].

droplet positioning and trapping in **Figure 9D**. A PTFE film with nano-sized bumpy structures could be fabricated by femtosecond laser ablation under ambient conditions. Then a superhydrophobic PDMS surface was easily replicated from the superhydrophobic PTFE mold owing to the tribological properties of PTFE. As a result, a superhydrophobic cage structure on a PDMS replica surface was prepared by laser enabled direct writing. The optical image of one superhydrophobic cage structure was shown in **Figure 9D**. Subsequently, dropping a liquid with colloidal particles on the surface of superhydrophobic PDMS, colloidal particles self-assembly in this superhydrophobic cage during evaporation process, forming a self-assembled PC.

Choi et al. [44] employed a fast, high-through method to fabricate size-tunable micro/nanoparticle clusters via evaporative assembly in picoliter-scale droplets of particle suspension on hydrophobic substrate. Various morphologies that particle clusters with accurate positioning

and alignment are demonstrated (shown in **Figure 10A** and **B**). the whole fabrication process includes: (i) Particle suspension menisci are extruded to the upfront end of the membrane by gravity. (ii) Contact of the head with the substrate is achieved. (iii) Surface tension of the substrate attracts a fraction of the suspension fluid. (iv) Picoliter-scale droplets are transferred to the substrate via pinch-off processes. (v) Rapid evaporative self-assembly of the particles forms 3-D clusters. In this case, the printing head was fabricated by the method of applying traditional microfabrication technology to SOI (Silicon-On-Insulator) substrates while a micro/nanoparticle suspension container was achieved by being wet-etched of backside. A microporous membrane with a 200 nm thickness was released on the head after the above whole process. After the suspension was loaded into the head, the meniscus of the droplet was completely extruded to the front of the head. Then, multiple picoliter-scale (2 − 20pL) droplet of particle suspension was transferred from the bulk suspension to the substrate by direct contact of the head with the substrate. This whole process could be achieved less than 5 s. The evaporative self-assembly process is controlled by gravity force and surface tension force of a contacting surface and controlled sizes and spacing of particle clusters.

Kim et al. [56] reported a novel and controllable patterning technique for 3D or 2D colloidal arrays of polymeric domes using photocurable emulsion droplets as templates (**Figure 10C–E**). The oil-in-water emulsion droplets will adhere selectively on the surface with a high interfacial affinity. The preparation process includes the following parts: first, a patterned glass substrate was prepared by microcontact printing with a hydrophobic ink of octadecyltrichlorosilane (OST). The OTS molecules binded covalently on the clean glass which from a poly(dimethylsiloxane) (PDMS) stamp. PDMS stamps had cylindrical posts of patterned arrays or characters by soft-lithography. Then, dropping oil-in-water emulsion in the surface of prepatterned glass substrate.

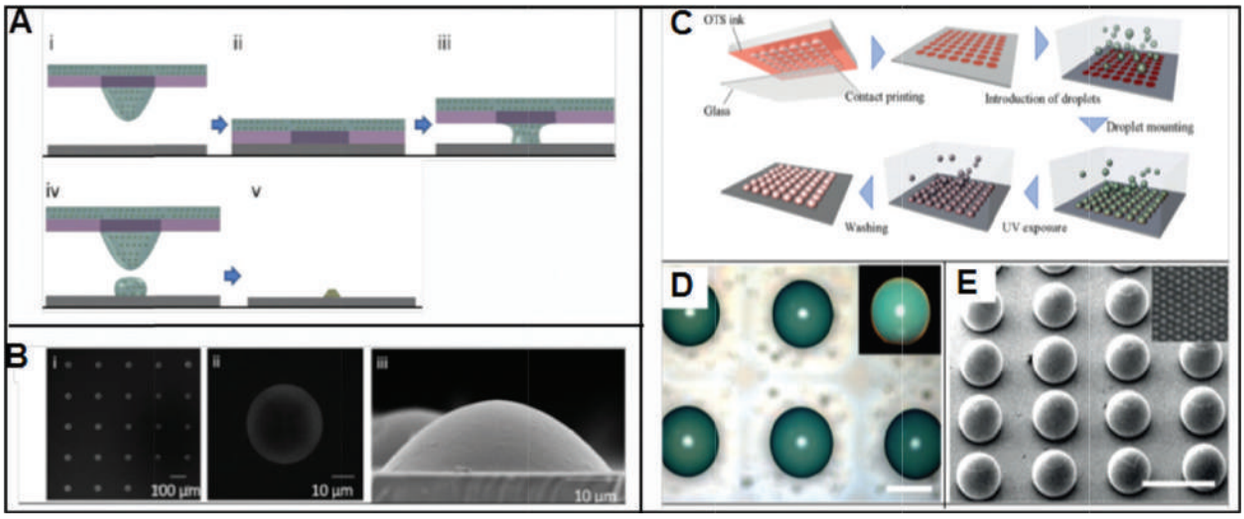

Figure 10. Schematics of printing procedure. (A) Serial processes for the fabrication of the PC sphere on hydrophobic substrate. (B) SEM views of zinc oxide nanoparticle (diameter ≈ 30 nm) clusters [44]. (C) Schematic of mounting and solidifying of droplets on a substrate pre-patterned with a hydrophobic moiety. (D) Optical microscopy images of patterned photonic domes of a 260-mm diameter with a 500-mm interval. They are composed of 170-nm silica particles (33 vol%) in an ETPTA matrix. (E) SEM image of the dome pattern; the inset shows the surface morphology of the dome. Scale bars, 500 μm [56].

The oil phase was ethoxylated trimethylolpropane triacrylate (ETPTA), which could be photocurabled. In water, a high CA of 158.4°for ETPTA on the bare glass was showed but it was inclined to spread over the OTS-coated glass with a low CA of 8°. As a result, the ETPTA drops could be selectively adsorbed on the patterned OTS dots. Finally, a pattern of hemispherical colloidal PC was prepared by using ETPTA droplets with SiO_2 particles. The as-prepared colloidal PC dome presented hexagonal arrangement of colloidal silica particles on its surface, which corresponded to the (111) plane of the FCC lattice.

Ultratrace detection is of enormous interest in early diagnosis, drugs testing, explosives detection, and ecopollution determination [57–60]. Fog collecting structure on Stenocara beetle's back gives a good example to fabricate a PC microchip with hydrophilic–hydrophobic micropattern by inkjet printing. It makes high-sensitive ultratrace detection of fluorescence analytes and fluorophore-based assays possible. For example, Hou et al. [20] prepared a PC microchip which was printed by the hydrophilic monodispersed poly(styrene-methylmethacrylate-acrylic acid) (poly(St-MMA-AA)) spheres on a hydrophobic polydimethylsiloxane (PDMS) substrate. All PC dots (**Figure 11A**) were about 200 mm in diameter. They were assembled from the monodispersed colloidal spheres with diameters of 180, 215, and 240 nm, named as PC_{180}, PC_{215}, and PC_{240}, respectively. The wettability between a PC dot and a PDMS substrate

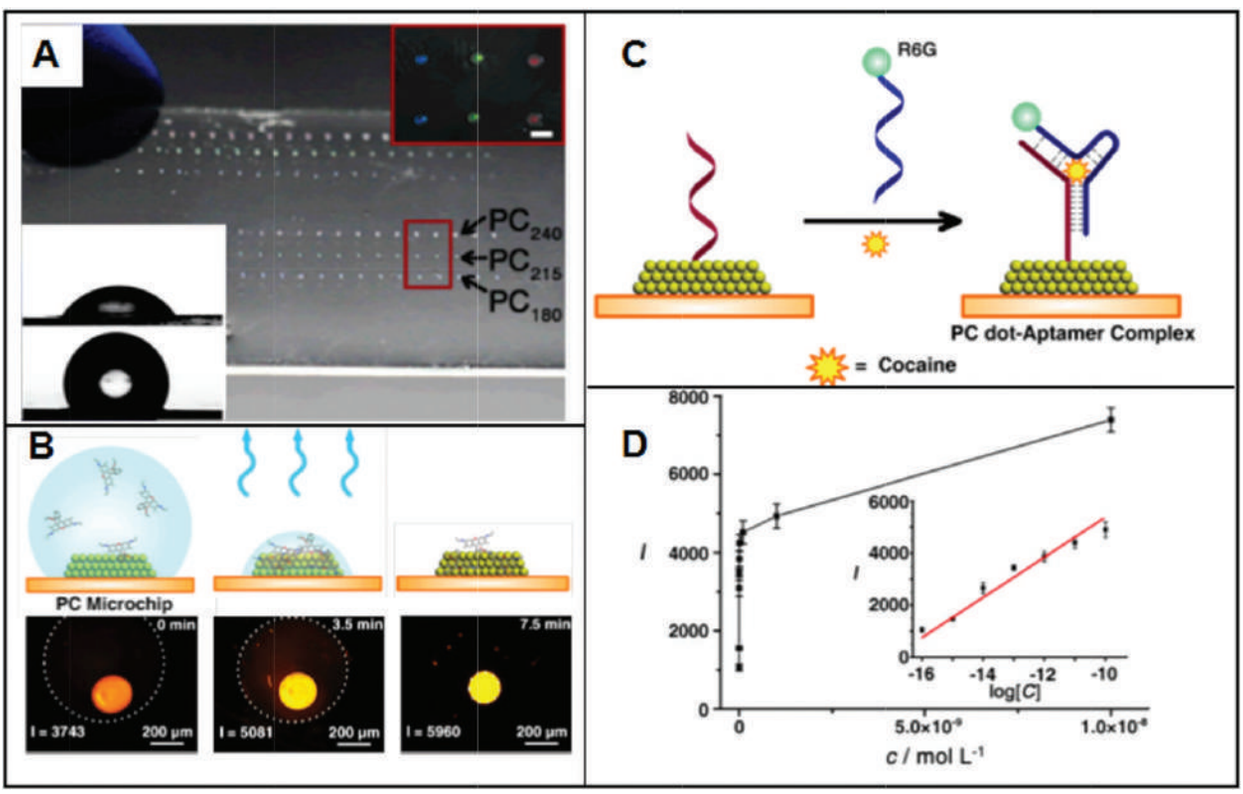

Figure 11. (A) Photography of the bio-inspired PC microchip with hydrophilic PC dots on hydrophobic substrate. The inset shows the magnified picture corresponding to PC dots of different stopbands. The scale bar is 200 mm. The CA of PDMS substrate is 115.0 ± 3.1° while CA of the PC dot was 46.4 ± 3.4°.(B) schematic representation of the cocaine detection mechanism and the fluorescence intensities at different cocaine concentrations. The inset shows a linear relationship between fluorescence intensity and the logarithm of the cocaine concentration (1×10^{-10} to 1×10^{-16} mol L^{-1}) [20].

is quite different. Because of hydrophilic-hydrophobic micropattern, the analyte in the highly diluted solution droplet can be concentrated onto the PC dot. This phenomenon is mainly due to the wettability difference between the hydrophilic PC dot and the hydrophobic PDMS substrate. The solution dewetted from the hydrophobic substrate and was concentrated to the hydrophilic PC dot with the water evaporation. In **Figure 11B**, the PC dot was functionalized with capture DNA. By enriching the cocaine molecules and the R6G-labeled target DNA from solution onto the PC dot, it was possible to detect cocaine. After enriching cocaine on the PC dot and specifically capturing by a DNA-functionalized PC dot and R6G-labeled target DNA, the high-efficient fluorescence detection could be realized (**Figure 11C** and **D**).

5. Conclusions

In conclusion, we presented a summarization about the influence of the substrate wettability on colloidal assembly. It is clear that the substrate with different wettability produces a distinct influence on the colloidal assembly process, the resultant assembly structure and the resulting functionality, it will bring about new insight for the creation of novel-type PC optic devices.

Author details

Junchao Liu, Jingxia Wang* and Lei Jiang

*Address all correspondence to: jingxiawang@mail.ipc.ac.cn

CAS, Key Laboratory of Bio-inspired Materials and Interface Sciences, Technical Institute of Physics and Chemistry Chinese Academy of Sciences, Beijing, China

References

[1] Yablonovitch E. Inhibited spontaneous emission in solid-state physics and electronics. Physical Review Letters. 1987;**58**:2059-2062. DOI: 10.1103/PhysRevLett.58.2059

[2] John S. Strong localization of photons in certain disordered dielectric superlattices. Physical Review Letters. 1987;**58**:2486-2489. DOI: 10.1103/PhysRevLett.58.2486

[3] Yablonovitch E. Photonic band-gap crystals. Journal of Physics: Condensed Matter. 1993;**5**:2443-2460. DOI: 10.1088/0953-8984/5/16/004

[4] Joannopoulos JD, Villeneuve PR, Fan SH. Photonic crystals: Putting a new twist on light. Nature. 1997;**386**:143-149. DOI: 10.1038/386143a0

[5] Fang Y, Ni YL, Leo SY, Taylor C, Basile V, Jiang P. Reconfigurable photonic crystals enabled by pressure-responsive shape-memory polymers. Nature Communications. 2015;**6**:7416. DOI: 10.1038/ncomms8416

[6] Liu JC, Wan L, Zhang MB, Jiang KJ, Song K, Wang JX, Ikeda T, Jiang L. Electrowetting-induced morphological evolution of metal-organic inverse opals toward a water-lithography approach. Advanced Functional Materials. 2017;**27**:1605221. DOI: 10.1002/adfm.201605221

[7] Burgess IB, Mishchenko L, Hatton BD, Kolle M, Loncar M, Aizenberg J. Encoding complex wettability patterns in chemically functionalized 3D photonic crystals. Journal of the American Chemical Society. 2011;**133**:12430-12432. DOI: 10.1021/ja2053013

[8] Teyssier J, Saenko SV, van der Marel D, Milinkovitch MC. Photonic crystals cause active colour change in chameleons. Nature Communications. 2015;**6**:6368. DOI: 10.1038/ncomms7368

[9] Qin M, Huang Y, Li YN, Su M, Chen BD, Sun H, Yong PY, Ye CQ, Li FY, Song YL. A rainbow structural-color Chip for multisaccharide recognition. Angewandte Chemie, International Edition. 2016;**55**:6911-6914. DOI: 10.1002/anie.201602582

[10] Sun XM, Zhang J, Lu X, Fang X, Peng HS. Mechanochromic photonic-crystal fibers based on continuous sheets of aligned carbon nanotubes. Angewandte Chemie, International Edition. 2015;**54**:3630-3634. DOI: 10.1002/anie.201412475

[11] Kuno T, Matsumura Y, Nakabayashi K, Atobe M. Electroresponsive structurally colored materials: A combination of structural and Electrochromic effects. Angewandte Chemie, International Edition. 2016;**55**:2503-2506. DOI: 10.1002/anie.201511191

[12] Yin SN, Yang SY, Wang CF, Chen S. Magnetic-directed assembly from Janus building blocks to multiplex molecular-analogue photonic crystal structures. Journal of the American Chemical Society. 2016;**138**:566-573. DOI: 10.1021/jacs.5b10039

[13] Ge JP, Yin YD. Responsive photonic crystals. Angewandte Chemie, International Edition. 2011;**50**:1492-1522. DOI: 10.1002/anie.200907091

[14] Li HL, Wang JX, Yang LM, Song YL. Superoleophilic and Superhydrophobic inverse opals for oil sensors. Advanced Functional Materials. 2008;**18**:3258-3264. DOI: 10.1002/adfm.200800507

[15] Ye XZ, Li Y, Dong JY, Xiao JY, Ma YR, Qi LM. Facile synthesis of ZnS Nanobowl arrays and their applications as 2D photonic crystal sensors. Journal of Materials Chemistry C. 2013;**1**:6112-6119. DOI: 10.1039/c3tc30118d

[16] Gur D, Palmer BA, Leshem B, Oron D, Fratzl P, Weiner S, Addadi L. The mechanism of color change in the neon tetra fish: A light-induced tunable photonic crystal Array. Angewandte Chemie, International Edition. 2015;**54**:12426-12430. DOI: 10.1002/anie.201502268

[17] Liu CH, Ding HB, ZQ W, Gao BB, FF F, Shang LR, ZZ G, Zhao YJ. Tunable structural color surfaces with visually self-reporting wettability. Advanced Functional Materials. 2016;**26**:7937-7942. DOI: 10.1002/adfm.201602935

[18] YN W, Li FT, Zhu W, Cui JC, Tao CA, Lin CX, Hannam PM, Li GT. Metal-organic frameworks with a three-dimensional ordered macroporous structure: Dynamic photonic materials. Angewandte Chemie, International Edition. 2011;**50**:12518-12522. DOI: 10.1002/anie.201104597

[19] Zhang YQ, Fu QQ, Ge JP. Photonic sensing of organic solvents through geometric study of dynamic reflection Spectrum. Nature Communications. 2015;**6**:7510. DOI: 10.1038/ncomms8510

[20] Hou J, Zhang HC, Yang Q, Li MZ, Song YL, Jiang L. Bio-inspired photonic-crystal microchip for fluorescent Ultratrace detection. Angewandte Chemie, International Edition. 2014;**53**:5791-5795. DOI: 10.1002/anie.201400686

[21] Vogel N, Belisle RA, Hatton B, Wong TS, Aizenberg J. Transparency and damage tolerance of Patternable Omniphobic lubricated surfaces based on inverse colloidal monolayers. Nature Communications. 2013;**4**:2176. DOI: 10.1038/ncomms3176

[22] Sano K, Kim YS, Ishida Y, Ebina Y, Sasaki T, Hikima T, Aida T. Photonic water dynamically responsive to external stimuli. Nature Communications. 2016;**7**:12559. DOI: 10.1038/ncomms12559

[23] Cubillas AM, Schmidt M, Euser TG, Taccardi N, Unterkofler S, Russell PS, Wasserscheid P, Etzold BJM. In situ heterogeneous catalysis monitoring in a hollow-Core photonic crystal fiber microflow reactor. Advanced Materials Interfaces. 2014;**1**:1300093. DOI: 10.1002/admi.201300093

[24] Mazingue T, Lomello TM, Hernandez RC, Passard M, Goujon L, Rousset JL, Morfin F, Bosselet F, Maulion G, Kribich R. Pellet photonic Innovant gas sensor using catalysis and integrated photonics. Sensors and Actuators B: Chemical. 2016;**222**:133-140. DOI: 10.1016/j.snb.2015.07.107

[25] Chen M, Zhang YP, Jia SY, Zhou L, Guan Y, Zhang YJ. Photonic crystals with a reversibly inducible and erasable defect state using external stimuli. Angewandte Chemie, International Edition. 2015;**54**:9257-9261. DOI: 10.1002/anie.201503004

[26] Chen K, Tuysuz H. Morphology-controlled synthesis of Organometal halide Perovskite inverse opals. Angewandte Chemie, International Edition. 2015;**54**:13806-13810. DOI: 10.1002/anie.201506367

[27] Fan J, Li YN, Bisoyi HK, Zola RS, Yang DK, Bunning TJ, Weitz DA, Li Q. Light-directing omnidirectional circularly polarized reflection from liquid-crystal droplets. Angewandte Chemie, International Edition. 2015;**54**:2160-2164. DOI: 10.1002/anie.201410788

[28] Gur D, Palmer BA, Weiner S, Addadi L. Light manipulation by guanine crystals in organisms: Biogenic Scatterers, mirrors, multilayer reflectors and photonic crystals. Advanced Functional Materials. 2017;**27**:1603514. DOI: 10.1002/adfm.201603514

[29] Lee SY, Choi JK, Jeong JR, Shin JH, Kim SH. Magnetoresponsive photonic microspheres with structural color gradient. Advanced Materials. 2017;**29**:1605450. DOI: 10.1002/adma.201605450

[30] Kim KH, Hwang MS, Kim HR, Choi JH, No YS, Park HG. Direct observation of exceptional points in coupled photonic-crystal lasers with asymmetric optical gains. Nature Communications. 2016;**7**:13893. DOI: 10.1038/ncomms13893

[31] Zhai Y, Ma YG, David SN, Zhao DL, Lou RN, Tan G, Yang RG, Yin XB. Scalable-manufactured randomized glass-polymer hybrid Metamaterial for daytime Radiative cooling. Science. 2017;**355**:1062-1066. DOI: 10.1126/science.aai7899

[32] Wu H, Kuang XH, Cui LY, Tian D, Wang MH, Luan GY, Wang JX, Jiang L. Single-material solvent-sensitive actuator from poly(ionic liquid) inverse opals based on gradient Gewetting. Chemical Communications. 2016;**52**:5924-5927. DOI: 10.1039/c6cc01442a

[33] Kralchevsky PA, Denkov ND. Capillary forces and structuring in layers of colloid particles. Current Opinion in Colloid & Interface Science. 2001;**6**:383-401. DOI: 10.1016/S1359-0294(01)00105-4

[34] Denkov ND, Velev OD, Kralchevsky PA, Ivanov IB, Yoshimura H, 2-Dimensional Crystallization NK. Nature. 1993;**361**:26-26. DOI: 10.1038/361026a0

[35] Tian Y, Jiang L. Wetting intrinsically robust hydrophobicity. Nature Materials. 2013;**12**:291-292. DOI: 10.1038/nmat3610

[36] Gu ZZ, Yu YH, Zhang H, Chen H, Lu Z, Fujishima A, Sato O. Self-assembly of Monodisperse spheres on substrates with different wettability. Applied Physics A: Materials Science & Processing. 2005;**81**:47-49. DOI: 10.1007/s00339-004-3020-4

[37] Sun ZJ, Bao B, Jiang JK, He M, Zhang XY, Song YL. Facile fabrication of a Superhydrophilic-superhydrophobic patterned surface by inkjet printing a sacrificial layer on a Superhydrophilic surface. RSC Advances. 2016;**6**:31470-31475. DOI: 10.1039/c6ra02170k

[38] Liu MJ, Wang JX, He M, Wang LB, Li FY, Jiang L, Song YL. Inkjet printing controllable footprint lines by regulating the dynamic wettability of coalescing ink droplets. ACS Applied Materials and Interfaces. 2014;**6**:13344-13348. DOI: 10.1021/am5042548

[39] Kuang MX, Wang JX, Bao B, Li FY, Wang LB, Jiang L, Song YL. Inkjet printing patterned photonic crystal domes for wide viewing-angle displays by controlling the sliding three phase contact line. Advanced Optical Materials. 2014;**2**:34-38. DOI: 10.1002/adom.201300369

[40] Cui LY, Zhang JH, Zhang XM, Li YF, Wang ZH, Gao HN, Wang TQ, Zhu SJ, HL Y, Yang B. Avoiding coffee ring structure based on hydrophobic silicon pillar arrays during single-drop evaporation. Soft Matter. 2012;**8**:10448-10456. DOI: 10.1039/c2sm26271a

[41] Kim SH, Lim JM, Jeong WC, Choi DG, Yang MY. Patterned colloidal photonic domes and balls derived from viscous Photocurable suspensions. Advanced Materials. 2008;**20**:3211-3217. DOI: 10.1002/adma.200800782

[42] Bao B, Li MZ, Li Y, Jiang KJ, ZK G, Zhang XY, Jiang L, Song YL. Patterning fluorescent quantum dot Nanocomposites by reactive inkjet printing. Small. 2015;**11**:1649-1654. DOI: 10.1002/smll.201403005

[43] Kawamura A, Kohri M, Yoshioka S, Taniguchi T, Kishikawa K. Structural color tuning: Mixing melanin-like particles with different diameters to create neutral colors. Langmuir. 2017;**33**:3824-3830. DOI: 10.1021/acs.langmuir.7b00707

[44] Choi S, Jamshidi A, Seok TJ, MC W, Zohdi TI. Fast, high-throughput creation of size-tunable micro/nanoparticle clusters via evaporative self-assembly in Picoliter-scale droplets of particle suspension. Langmuir. 2012;**28**:3102-3111. DOI: 10.1021/la204362s

[45] Ding HB, Zhu C, Tian L, Liu CH, Fu GB, Shang LR, Gu ZZ. Structural color patterns by Electrohydrodynamic jet printed photonic crystals. ACS Applied Materials and Interfaces. 2017;**9**:11933-11941. DOI: 10.1021/acsami.6b11409

[46] Qin M, Huang Y, Li YN, Su M, Chen BD, Sun H, Yang PY, Yang CQ, Li FY, Song YL. A rainbow structural-color Chip for multisaccharide recognition. Angewandte Chemie, International Edition. 2016;**55**:6911-6914. DOI: 10.1002/anie.201602582

[47] Rastogi V, Melle S, Calderón OG, GarcÍa AA, Marquez M, Velev OD. Synthesis of light-diffracting assemblies from microspheres and nanoparticles in droplets on a Superhydrophobic surface. Advanced Materials. 2008;**20**:4263-4268. DOI: 10.1002/adma.200703008

[48] Rastogi V, GarcÍa AA, Marquez M, Velev OD. Anisotropic particle synthesis inside droplet templates on Superhydrophobic surfaces. Macromolecular Rapid Communications. 2010;**31**:190-195. DOI: 10.1002/marc.200900587

[49] Zhou JM, Yang J, Gu ZD, Zhang GF, Wei Y, Yao X, Song YL, Jiang L. Controllable fabrication of noniridescent microshaped photonic crystal assemblies by dynamic three-phase contact line behaviors on Superhydrophobic substrates. ACS Applied Materials and Interfaces. 2015;**7**:22644-22651. DOI: 10.1021/acsami.5b07443

[50] Huang Y, Zhou JM, Su B, Shi L, Wang JX, Chen SR, Wang LB, Zi J, Song YL, Jiang L. Colloidal photonic crystals with narrow Stopbands assembled from low-adhesive Superhydrophobic substrates. Journal of the American Chemical Society. 2012;**134**:17053-17058. DOI: 10.1021/ja304751k

[51] Gu ZZ, Fujishima A, Sato O. Patterning of a colloidal crystal film on a modified hydrophilic and hydrophobic surface. Angewandte Chemie, International Edition. 2002;**4**:2068-2070. DOI: 10.1002/1521-3757

[52] Lee SW, Na YJ, Choi Y, Lee SD. Site-selective assembly and fixation of colloidal particles into two-dimensional Array on wettability-patterned surface. Japanese Journal of Applied Physics. 2007;**46**:1129-1131. DOI: 10.1143/JJAP.46.L1129

[53] Wu L, Dong ZC, Kuang MX, Li YN, Li YF, Jiang L, Song YL. Printing patterned fine 3D structures by manipulating the three phase contact line. Advanced Functional Materials. 2015;**25**:2237-2242. DOI: 10.1002/adfm.201404559

[54] Wang YZ, Wei C, Cong HL, Yang Q, Wu YC, Su B, Zhao YS, Wang JX, Jiang L. Hybrid top-down/bottom-up strategy using Superwettability for the fabrication of patterned colloidal assembly. ACS Applied Materials and Interfaces. 2016;**8**:4985-4993. DOI: 10.1021/acsami.5b11945

[55] Yoo JH, Kwon HJ, Paeng D, Yeo J, Elhadj S, Grigoropoulos CP. Facile fabrication of a superhydrophobic cage by laser direct writing for site-specific colloidal self-assembled photonic crystal. Nanotechnology. 2016;**27**:145604. DOI: 10.1088/0957-4484/27/14/145604

[56] Kim SH, Kim SH, Yang SM. Patterned polymeric domes with 3D and 2D embedded colloidal crystals using Photocurable emulsion droplets. Advanced Materials. 2009;**21**: 3771-3775. DOI: 10.1002/adma.200901243

[57] Arya SK, Bhansali S. Lung cancer and its early detection using biomarker-based biosensors. Chemical Reviews. 2011;**111**:6783-6809. DOI: 10.1021/cr100420s

[58] Apple FS, Smith SW, Pearce LA, Ler R, Murakami MM. Use of the centaur TnI-ultra assay for Ddetection of myocardial infarction and adverse events in patients presenting with symptoms suggestive of acute coronary syndrome. Clinical Chemistry. 2008;**54**:723-728. DOI: 10.1373/clinchem.2007.097162

[59] Steinfeld JI, Wormhoudt J. Explosives detection: A challenge for physical chemistry. Annual Review of Physical Chemistry. 1998;**49**:203-232. DOI: 10.1146/annurev.physchem.49.1.203

[60] Zhang HX, Hu JS, Yan CJ, Jiang L, Wan L. Functionalized carbon nanotubes as sensitive materials for electrochemical detection of ultra-trace 2,4,6-trinitrotoluene. Physical Chemistry Chemical Physics. 2006;**8**:3567-3572. DOI: 10.1039/b604587c

Chapter 6

The Dawn of Photonic Crystals: An Avenue for Optical Computing

Renju Rajan, Padmanabhan Ramesh Babu and Krishnamoorthy Senthilnathan

Additional information is available at the end of the chapter

http://dx.doi.org/10.5772/intechopen.71253

Abstract

In this chapter, a new paradigm is developed for optical computation using photonic crystals. As photonic crystals are the most sophisticated optical materials to date, information processing using this structure is one of the most sought-after technologies in photonics. While the semiconductor industry is striving hard to increase the microprocessors' processing power, it is certain that the trend would not last forever as against Moore's prediction. At this juncture, photonics technologies have to compete with the upcoming quantum computing technology to emerge as a promising successor for semiconductor microprocessors. This chapter is devoted to the introduction of photonic crystals as the workhorse for an all-optical computational system with a myriad of logic gates, memory units, and networks which can be constructed using these structures.

Keywords: optical computing, optical logic gates, optical memory, nanocavity, optical Kerr effect

1. Introduction

Modern computers evolved out of the semiconductor technology which began with the invention of transistor in 1948 [1]. Compared to previous generation of computers which used vacuum tubes, transistors were smaller, reliable, and efficient. In a subsequent development, integrated circuit which incorporates several transistors into a single chip was invented in 1958 [2]. This was a real revolution for the semiconductor technology which has enabled scalability of the processing power with an increase in the number of transistors that are inducted into the chip. In addition, these chips consume less power, run faster, and are smaller than their transistor counterparts. With an ever-increasing demand for processing power, there is a corresponding increase in demand for fabricating chips with more and more transistors in them. This has resulted in miniaturization of the individual transistor components in the chip,

which has now crossed into the nano regime [3]. This trend is supposed to end somewhere in the near future, due to the size of individual components reaching the size of individual atoms. This roadblock in semiconductor technology can be solved by embracing alternative technologies such as optical computing.

Ever since the advent of lasers, there have been deliberate efforts to develop an optical analog for computation. Optical computation was initially envisaged as a hybrid system consisting of electronic and optical components. This venture turned out to be unsuccessful due to the unfeasible conversion time required from one system to another [4]. Even today, this is a daunting task, provided the communication networks are all made of optical fibers. However, the processing part is currently done by semiconductor microprocessors. With the introduction of photonic crystals, there is again a renewed interest in an otherwise dropped plan of optical computation. Photonic crystals have got the potential to create an all-optical information processing system. This will have an overwhelming influence on the information processing capacity of the communication system as a whole. In this chapter, an overview of such an optical computational system which can be implemented using a photonic crystal is outlined. An introduction to computer architecture is given in Section 2. The basics of planar photonic crystals are described in Section 3. The implementation of logic gates using photonic crystals is discussed in Section 4. An optical memory unit which can be implemented using photonic crystals is delineated in Section 5. The chapter is concluded in Section 6.

2. Computer architecture

Computer architecture deals with the design which stipulates the working of a computer with its components such as microprocessor, memory, and input/output devices [5]. Ever since the introduction of von Neumann architecture in 1945 for the computer called EDVAC, it has been the de facto architecture for electronic computers for the subsequent generations to date [6]. Although the discussion in this section centers on this architecture, one cannot be sure if the future optical computers would continue to lean on this architecture. For the first time, the von Neumann architecture embarked on the concept of stored program for realizing a general purpose computer. This enabled the computer to perform different computational tasks based on the program stored in its memory. Other salient features of this architecture include the usage of binary digits and sequential execution of instructions from a given program. Major components of von Neumann architecture consist of central processing unit (CPU), memory unit, and input/output units. The general outline of von Neumann architecture is shown in **Figure 1**.

In a modern computer, microprocessor occupies the position of central processing unit by handling data processing and system control [7]. The data processing part is done by arithmetic/logic unit and register array of the microprocessor, whereas the system control is done by the control unit. Primitive computers had these units separately, but with the advancement in circuit integration technology, it is possible to incorporate them onto a single chip. A microprocessor takes data from input devices such as keyboard and mouse, processes those data

http://dx.doi.org/10.5772/intechopen.71253

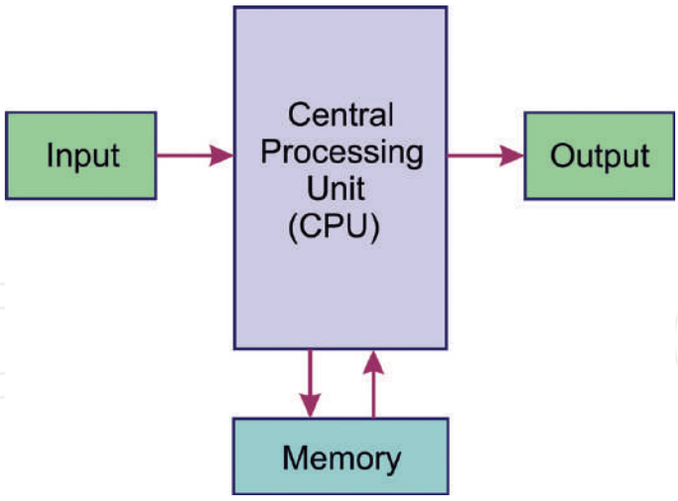

Figure 1. Outline of von Neumann architecture for computer.

according to the instructions stored in the memory, and sends the processed data into an output device such as monitor [8]. In this process, the data and control signals are transferred between microprocessor, memory, and input/output devices through a communication network known as the system bus. A typical microprocessor operation consists of fetch-execute cycles. A microprocessor fetches an instruction from the memory and executes that instruction on the input data. Afterward, it goes to the next instruction in the memory, fetches, and executes it. This process goes on until the last instruction before finishing a given task according to the program stored in the memory.

3. Planar photonic crystals

Photonic crystals (PhCs) are artificial periodic structures made of dielectric materials [9]. They are generally classified into three categories based on the dimensionality of the structure—1D, 2D, and 3D. Two dimensional structures such as planar photonic crystals, which are useful in integrated photonic circuits, are considered here for discussion. In these structures, air holes are arranged periodically across the plane of the structure such that the spacing between them is less than the wavelength of light propagating through them [10]. This causes light to reflect away from the air hole structure when trying to pass through them. On the other hand, light can propagate through a channel made within this structure with width more than the wavelength of light [11]. In some ways, this is analogous to cutting a road for transportation. This type of light localization feasible within these structures has made them suitable for integrated photonics circuits. Similar to optical fibers used in communication, these structures also exhibit very low loss for the passage of light as against the case of their electronic counterparts [12]. In this way, this technology is an energy efficient alternative for integrated circuits with minimal heat loss. A schematic representation of PhC slab with channel for light passage is shown in **Figure 2**.

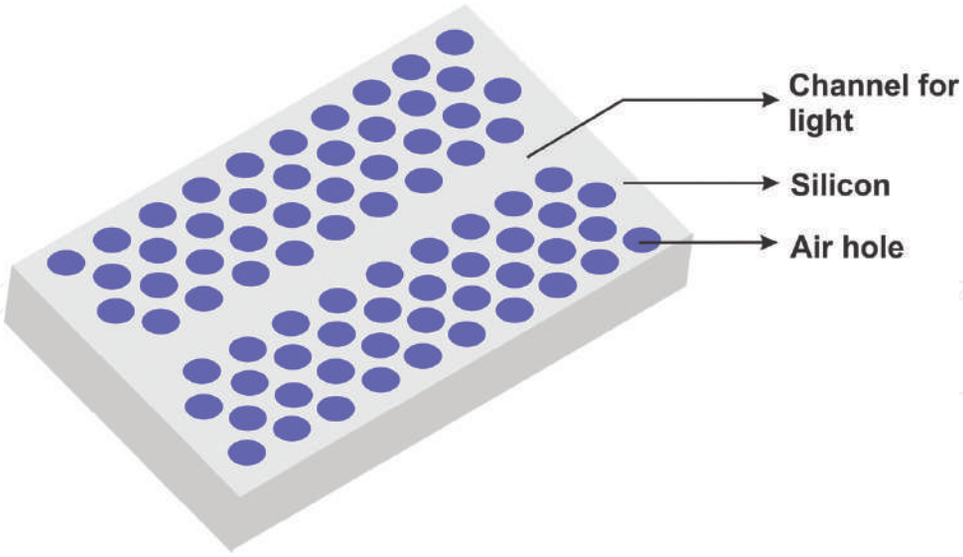

Figure 2. Schematic representation of photonic crystal slab with channel for light passage.

3.1. Structure of photonic crystal slabs

Photonic crystal slab is a planar structure made of silicon or other compound semiconductor material with periodically varying refractive index [13]. Toward this goal, air holes are etched in these structures such that a photonic band gap (PBG) is formed for certain wavelengths at which light cannot propagate through this structure. For these wavelengths, when some defects are created within the structure by disturbing the periodicity, light can be channelized through them with little propagation loss [14]. This is the working principle of a PhC slab. The PBG formation in a periodically varying refractive index structure is analogous to band gap formation for electrons in a crystal structure with Bragg diffraction from multiple ion lattice sites [15]. In planar photonic crystals, the Bragg diffraction is due to the periodic variation in refractive index by air holes. The PBG formed in a planar photonic crystal is not three dimensional. Rather, the band formed in it is two dimensional. In this way, there is light confinement for a defect in the horizontal plane of the PhC slab, whereas the vertical directions remain unconfined [16]. This can give rise to loss along the vertical directions. To do away with this loss, total internal reflection with the underlying silica or air layer is sought such that the light is confined within the structure [17]. Accordingly, for a silicon PhC slab, two types of structures are possible, one with silica and another with air as the underlying medium, as shown in **Figure 3**.

3.2. Nanocavities in photonic crystal slabs

Similar to a line defect which creates a channel waveguide, a point defect can create a nanocavity in the PhC slab structure [18]. Due to the requirement of tight light confinement in the vertical directions, an air-cladding photonic crystal structure having high refractive index contrast with the slab is preferred to a silica cladding for realizing a nanocavity [19]. A nanocavity can be created in a PhC slab by various means. It can be realized by creating a point defect, a line defect, or a width-modulated line defect in a photonic crystal [20]. A fourth method is also in practice wherein a double heterostructure results in a nanocavity. Each one of these

http://dx.doi.org/10.5772/intechopen.71253

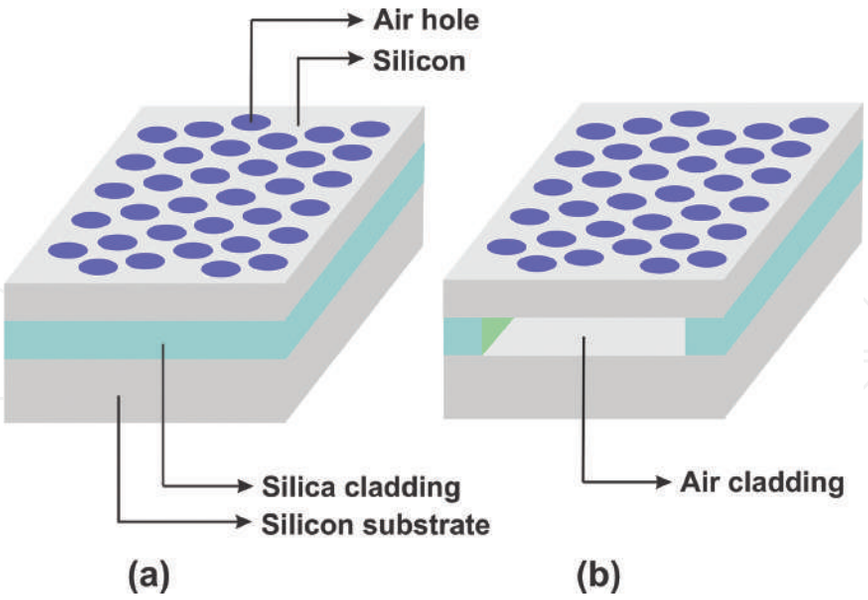

Figure 3. Schematic diagrams of two classes of photonic crystal slab structures, (a) with silica as the cladding layer and (b) with air as the cladding layer.

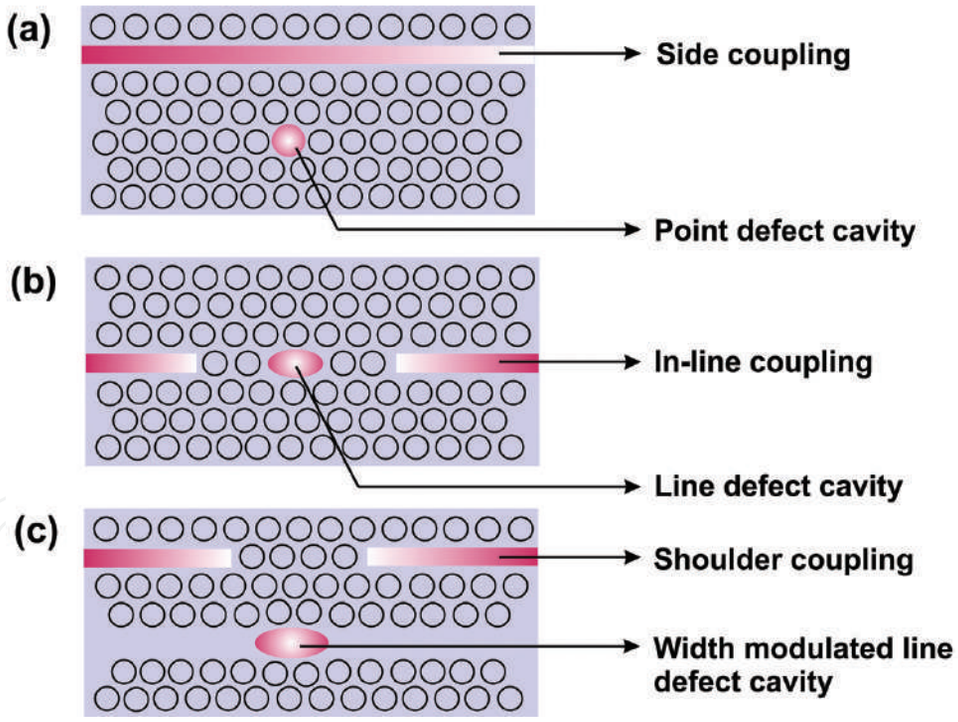

Figure 4. Schematic representation of nanocavities along with various coupling schemes: (a) a point-defect nanocavity with side coupling with the waveguide, (b) a line-defect nanocavity with in-line coupling with the waveguide, and (c) a width-modulated line defect nanocavity with shoulder coupling with the waveguide.

nanocavities is illustrated in **Figure 4**. For a point-defect nanocavity, a slight shift of the air holes from their regular positions away from the cavity region is found to produce significant increase in the Q factor of the cavity. Similarly, for a line defect cavity, a shift in the end holes

away from the cavity region offers an appreciable increase in the Q factor. Among these configurations, width-modulated line defect cavity and double-heterostructure cavity offer the highest Q factors and are the preferred configurations for nanocavity-based applications. There are various coupling schemes for coupling a nanocavity with a channel waveguide. Of these, side coupling, in-line coupling, and shoulder coupling schemes which are commonly in use are represented in **Figure 4**.

3.3. Fabrication of photonic crystal slabs

PhC slabs can be fabricated using electron beam lithography or UV lithography technique [21]. While electron beam (e-beam) lithography is suitable for fabrication on a laboratory scale, UV lithography suits to the requirements for mass production. In both schemes, there are a series of steps to be followed for realizing a PhC slab with an air cladding. For silicon PhC slabs, the readily available SOI (silicon-on-insulator) wafer used in semiconductor industry is used as a substrate for realizing PhC slabs [22, 23]. On the other hand, for compound semiconductors, the substrates have to be custom-made in the laboratory [24]. The process steps involved in the fabrication of silicon PhC slabs are considered here. Initially, the SOI wafer is coated with an e-beam resist such as polymethyl methacrylate (PMMA). The pattern that has to be imprinted is transferred from a CAD onto the surface of the resist using an e-beam. The resist is sensitive to e-beam, and the exposed parts of the resist are subsequently removed using chemicals in the development stage. This process is analogous to photographic film development in analog photography. The resulting resist which contains holes at lattice points serves as a template for the subsequent etching process on SOI. After etching is done in the silicon layer, the resist and the underneath silica layer are removed to form the air-cladding PhC slab. These process steps involved in the fabrication of silicon PhC slabs are illustrated in **Figure 5**.

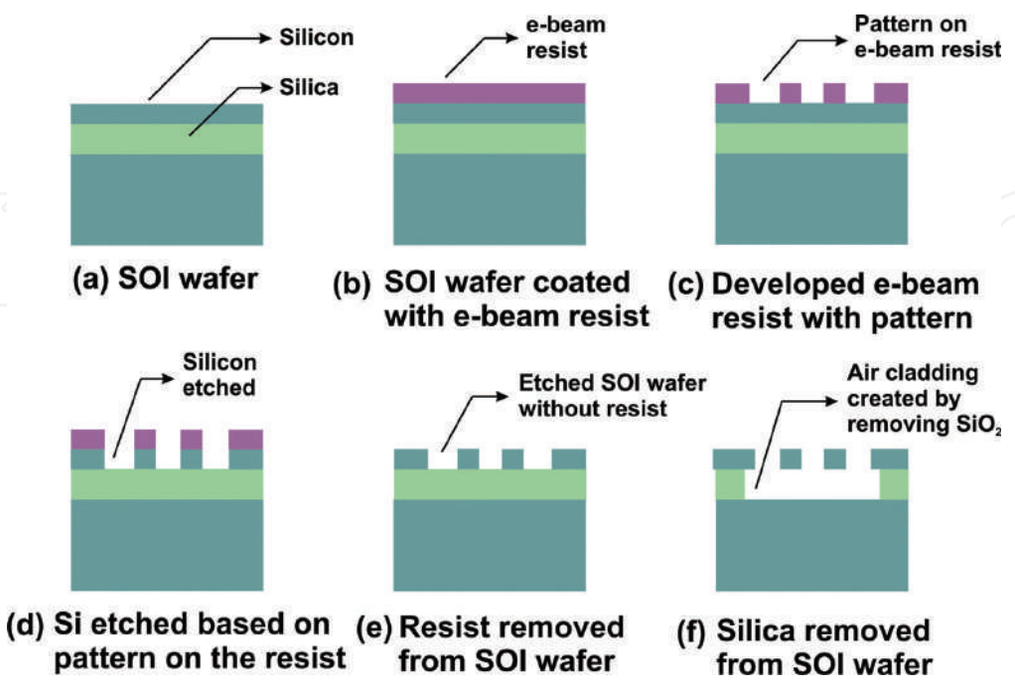

Figure 5. Series of process involved in the fabrication of silicon photonic crystal slabs.

4. Logic gates using photonic crystals

Many of the phenomena in optics can very well be described within the framework of wave theory of light based on Maxwell's equations, without resorting to the complexity of quantum mechanics. Even today, this is the preeminent theory which stands out against the test of time [25]. Nonlinear optics which is an offshoot of classical electrodynamics is also a branch of optics. Even though nonlinearity is routine in electronic devices such as diodes and transistors, it was not so in optics until the invention of laser. Laser, due to its high intensity, can have electric field strength comparable to bond strength between atoms, resulting in nonlinear response from the optical materials through which it propagates [26]. The nonlinear response from the medium can be modeled by taking into account of the Taylor series expansion of the electric field of the laser light. This can be explicitly represented in terms of polarization of the medium, wherein higher order terms in series describe the nonlinear polarization [27],

$$P(E) = \varepsilon_0\left(\chi_1 E + \chi_2 E^2 + \chi_3 E^3 + \cdots\right), \tag{1}$$

where first term denotes linear polarization, and higher order terms represent nonlinear polarization. Here, E is electric field strength, ε_0 is permittivity in free space, and $\chi_1, \chi_2, \chi_3, \ldots$ denote first-order, second-order, and third-order electric susceptibilities, and so on. Eq. (1) can be used for describing various nonlinear optical processes which can occur in a system. Accordingly, first-order term in Eq. (1) is responsible for linear polarization, second-order term is responsible for second harmonic generation, and third-order term is responsible for third harmonic generation, optical Kerr effect, and so on. Optical Kerr effect is responsible for change in refractive index corresponding to intensity of the light source [28]. Intensity dependent refractive index is expressed as,

$$n(I) = n_0 + n_2 I, \tag{2}$$

where n_0 is the linear refractive index and n_2 is the nonlinear refractive index coefficient. The value of n_2 can be positive or negative depending on the type of material. Thus, for a material with positive n_2, the overall refractive index increases and vice versa. The intensity dependent variation in refractive index can be used for making optical logic gates. But, in this approach, the nonlinearity of the medium turns out to be crucial as it relates to the operation of the logic gates. Hence, materials with high nonlinearity are preferred to those with weak nonlinearities. Since nonlinearity of silicon is very low when compared to other compound semiconductors, it may not be the suitable candidate for realizing such all-optical logic gates [29]. Further, with the materials of high nonlinearity, deploying ultrashort pulses down to femtosecond range results in faster switching [30]. In this way, nonlinear response of the medium can be put to good use for realizing logic gates in PhC slabs.

4.1. NOT gate in a photonic crystal

Logic gates are fundamental building blocks of a digital computer [31]. Basic logic operations such as NOT, AND, OR, as well as their derivatives can be generated using these digital circuits. Truth table of a logic circuit represents the output of the circuit under various conditions of input. The truth table and circuit symbol of a NOT gate are shown in **Figure 6(a)**. It is possible to carry

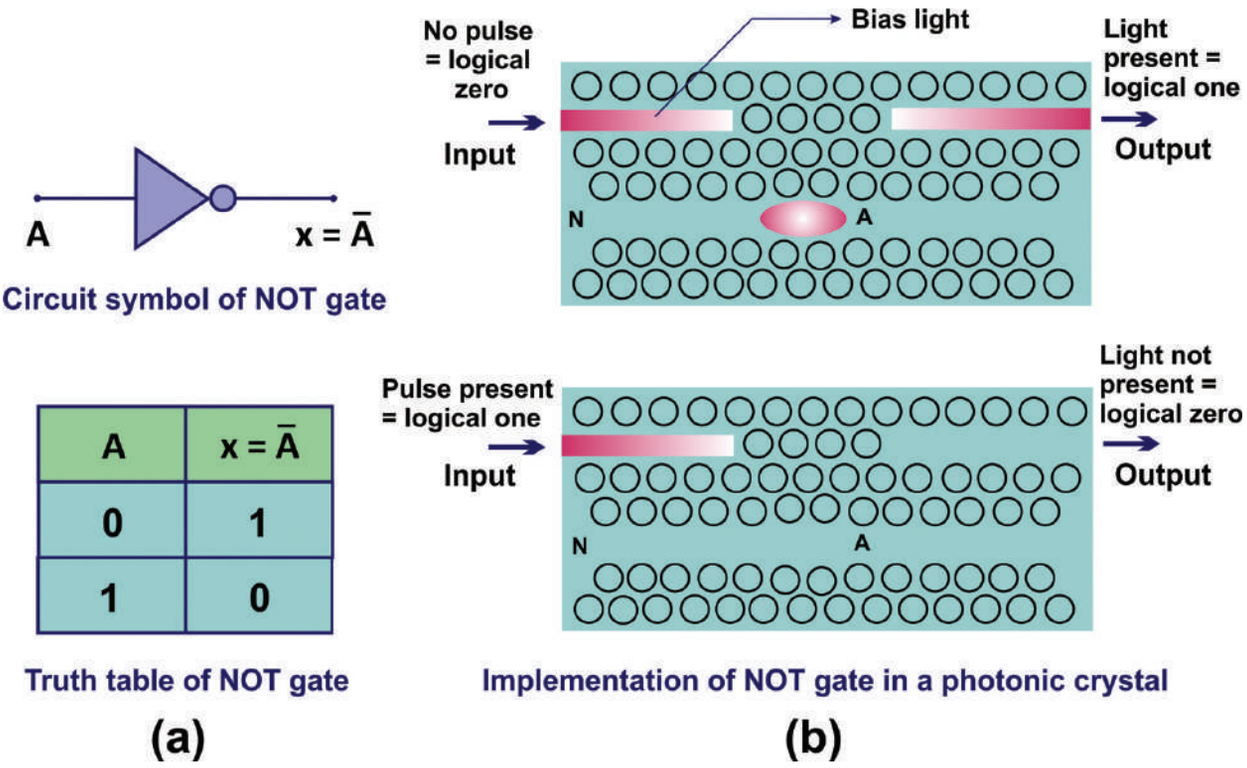

Figure 6. (a) Circuit symbol and truth table of a NOT gate and (b) implementation of NOT operation using a photonic crystal slab.

out the inverting operation done by the NOT gate using a PhC slab by exploiting the optical nonlinearity. A nonlinear medium with negative value for n_2 can be used for achieving this goal as shown in **Figure 6(b)**. Here, the coupling between the waveguide and nanocavity is such that when there is no optical pulse at the input waveguide, the bias light would emerge at the output waveguide. On the other hand, when an optical pulse is passed through the input waveguide, refractive index of the medium gets reduced due to negative nonlinearity of the medium. As a result, the resonant wavelength of the resonator differs considerably from the input wavelength of the bias light, resulting in decoupling of the bias light from the nanocavity and the output waveguide. In this way, the requirement of a NOT gate can be satisfied using this design, wherein the presence of an optical pulse at the input end gives no light at the output, and the absence of an optical pulse gives light at the output end of the waveguide. Here, the presence of a pulse at the input waveguide denotes a logic one, and the absence of a pulse denotes a logical zero. The same can also be implemented using materials with positive value for n_2.

It would be useful to adopt some naming conventions before dwelling further into the topic. In this regard, it is useful to note that there are two types of nonlinear media, one with positive Kerr nonlinearity (n_2 is positive) and the other with negative Kerr nonlinearity (n_2 is negative). Here, these two nonlinearities are represented in the sketch of PhC slab by **P** and **N**, respectively. In the sketches, a lighter shade is used to represent a material with positive Kerr nonlinearity, whereas the one with a darker shade represents negative Kerr nonlinearity. Moreover, based on the resonance wavelength of the nanocavity, three types of cavities are possible. A cavity having resonance at the same wavelength as that of the input light is denoted by **A** in the sketch, whereas a cavity with resonance wavelength lower than the input

http://dx.doi.org/10.5772/intechopen.71253

light is denoted by **L,** and a cavity whose resonance wavelength is set higher than the input light is denoted by **H** in the sketch. When an incoming radiation satisfies the resonance condition of the cavity [32],

$$2nd = p\lambda, \tag{3}$$

it is allowed to pass through the cavity. In other cases, the cavity would block the passage of light through it. In Eq. (3), d is cavity length, λ is wavelength of light, p is an integer, and n is the refractive index of the medium within the cavity given by Eq. (2). From this equation, it is clear that the resonance wavelength of the cavity is decided by the cavity length and refractive index of the medium. A cavity can be designed such that a slight deviation from the resonance cavity length can be compensated by the variation in refractive index due to the optical Kerr effect. In this way, when the refractive index of the medium gets altered by the input pulse, the resonance condition of the cavity sets in, allowing the passage of light through the cavity. When there is no input light pulse, resonance condition of the cavity is disturbed, resulting in blockage of the light. This is the working principle of a cavity-based optical switching circuit. In total, two types of nonlinearities along with three types of cavity configurations result in six possible combinations. Of these, four can be put to good use for creating logic gates.

4.2. OR gate in a photonic crystal

For an OR gate, the output is a logical one even if either of the inputs is a logical one. It gives a logical zero only when all of the inputs are at logical zero. For two inputs A and B, the OR logical operation is expressed by A + B. The circuit symbol and truth table of an OR gate are given in **Figure 7(a)**. This logical operation can be implemented in a PhC slab by using a combination of three nanocavities as shown in **Figure 7(b)**. Here, the PhC slab is made of

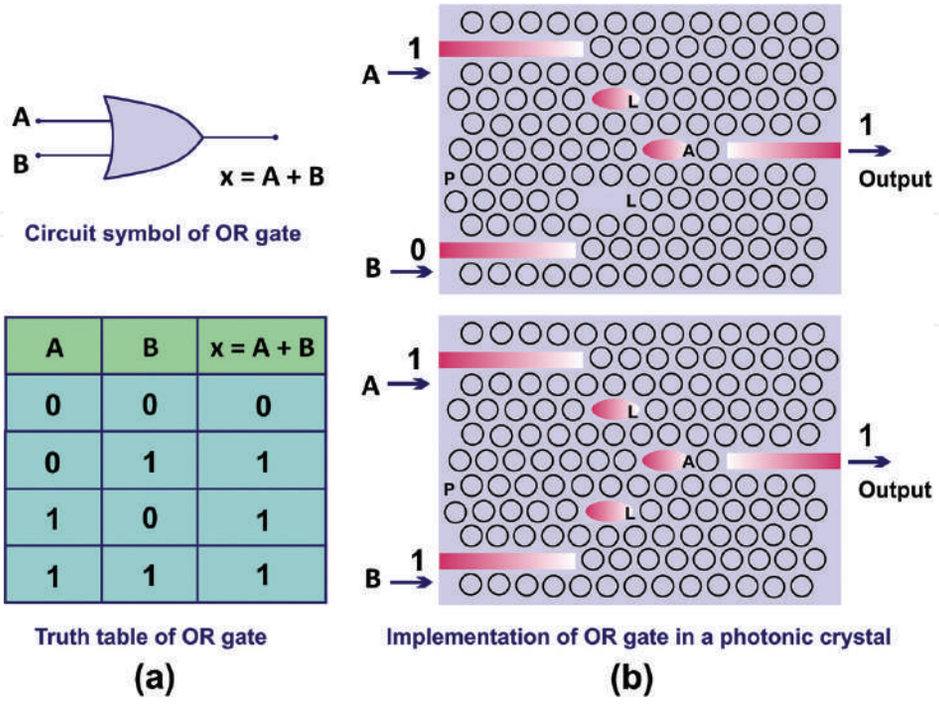

Figure 7. (a) Circuit symbol and truth table of OR gate and (b) implementation of OR gate operation in a photonic crystal slab.

material with positive Kerr nonlinearity. But, it can also be implemented using a material with negative Kerr nonlinearity too. The nanocavities adjacent to the input waveguides are set to have resonance at wavelengths below the input wavelength of light. In this way, they are opaque when there is no input pulse. On the other hand, when a pulse is sent through the input waveguide, there is an increase in local refractive index due to optical Kerr effect, and as a result, the **L** cavities are set to resonance such that the light reaches the output waveguide through the **A** cavity. This can occur when a pulse is sent through both or either of the input waveguides. Thus, the arrangement of nanocavities in this manner helps mimic the operation of an OR gate in a PhC slab.

4.3. AND gate in a photonic crystal

For an AND gate, the output can go to logical one only, when all the inputs are at logical one. For the rest of the cases, the output of an AND gate turns out to be logical zero. The circuit symbol and truth table of an AND gate are shown in **Figure 8(a)**. For two inputs A and B, AND logical operation is expressed by A · B. It is possible to achieve AND operation with a proper combination of NOT and OR gates. This is the usual practice in digital circuits wherein the universal gates such as NOR and NAND are used for creating other gates. This insight stems from De Morgan's theorem in Boolean algebra which is at the very basis of digital circuitry. Accordingly, the implementation of an AND gate using NOR gates is shown in **Figure 8(b)** [31]. An optical logic circuit can also be constructed along the same lines using nanocavities in a PhC slab.

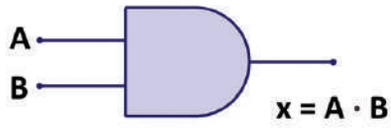

Circuit symbol of AND gate

A	B	x = A · B
0	0	0
0	1	0
1	0	0
1	1	1

Truth table of AND gate

(a)

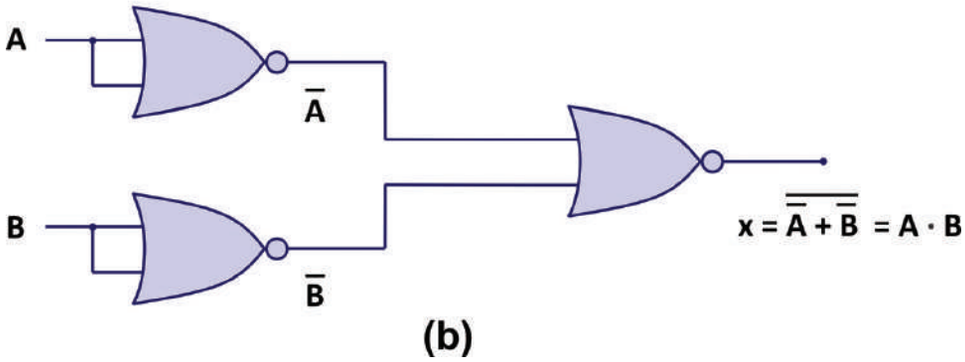

(b)

Figure 8. (a) Circuit symbol and truth table of AND gate and (b) implementation of AND operation using NOR gates.

http://dx.doi.org/10.5772/intechopen.71253

5. Optical memory using photonic crystals

Memory unit in a computer stores data and instructions required by a microprocessor for execution. For a modern digital computer, there are two types of memories, namely, a main memory which communicates directly with the microprocessor and an auxiliary memory which serves as a secondary storage [33]. Data and programs in auxiliary memory are brought into the main memory before being executed by the microprocessor. An efficient memory unit is required for increasing the performance of a computer. A microprocessor can locate memory addresses of a main memory using the address bus and transfer data through the data bus. Usually, the main memory which stores the data as electric charge in capacitors are volatile and cannot store data for more than few milliseconds due to the discharge of capacitor within this period. So, they need to be refreshed regularly to store data continuously. An optical analog of capacitors for storing data can be created in a PhC slab by using nanocavities [34, 35]. The scheme is similar to implementation of NOT gate discussed in the previous section. Here, the memory device is capable of achieving optical bistability as a result of optical Kerr nonlinearity-induced switching process [36]. The nanocavity can be set to resonance by the input pulse denoting a logical one, whereas the withdrawal of the pulse distorts the resonance which resets the cavity back to the logical zero state. Whenever the cavity is set to resonance, there is light at the output waveguide, denoting the logical one state of the cavity and vice versa. Light at the output waveguide can be used for identifying the instantaneous state of the cavity. In this way, nanocavities in a PhC slab can be used for storing digital data. The working of nanocavity-based memory device is illustrated in **Figure 9**.

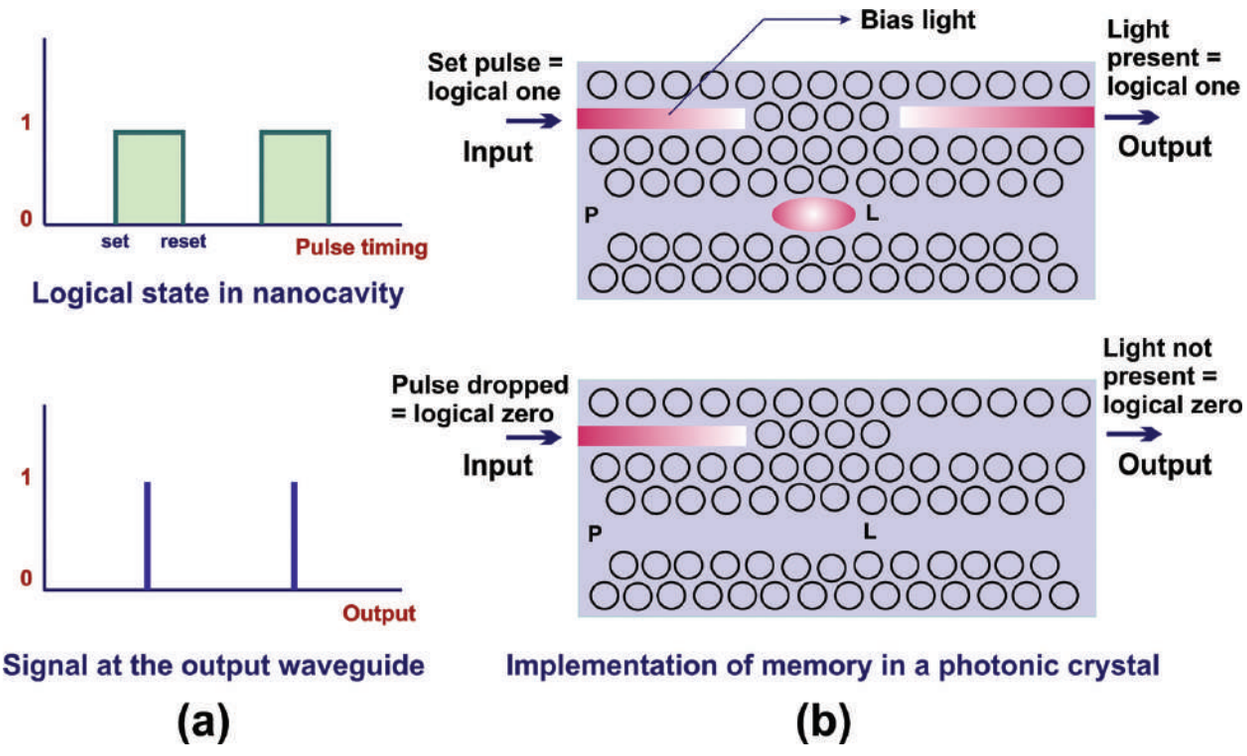

Figure 9. (a) Logical state of nanocavity and its indication in the output waveguide, and (b) implementation of memory in photonic crystal.

6. Conclusion

In this chapter, the implementation of an all-optical computational system has been delineated using photonic crystal slabs. Following the introduction to the computer architecture which comprises of microprocessor, memory, and input/output devices, the implementation of the same using photonic crystal slabs has also been discussed. Further, we have demonstrated optical logic operations in photonic crystals using optical nanocavities which can be created in these structures. The key feature which decides the working of photonic crystal slab-based logic gates is the change in refractive index which arises due to the optical Kerr effect upon the passage of laser pulses. An attempt has also been made for creating optical memory in photonic crystals, wherein resonance condition decides the logical state inside the cavity. Photonic crystal slabs with nanocavity-enabled logic gates and memory units can be used for constructing an all-optical information processor analogous to semiconductor microprocessors.

Acknowledgements

This work was inspired by the video "Photonic crystal optical bit memory" by NTT Basic Research Laboratories, Japan.

Author details

Renju Rajan, Padmanabhan Ramesh Babu and Krishnamoorthy Senthilnathan*

*Address all correspondence to: senthee@gmail.com

Department of Physics, School of Advanced Sciences, VIT University, Vellore, Tamil Nadu, India

References

[1] Null L, Lobur J. The Essentials of Computer Organization and Architecture. Sudbury: Jones and Bartlett Publishers; 2003

[2] Jiles D. Introduction to the Electronic Properties of Materials. Dordrecht: Springer Science + Business Media; 1994

[3] Brey BB. The Intel Microprocessors: 8086/8088, 80186/80188, 80286, 80386, 80486, Pentium, Pentium pro Processor, Pentium II, Pentium III, Pentium 4, and Core2 with 64-Bit Extensions: Architecture, Programming, and Interfacing. 8th ed. Columbus: Pearson Education; 2009

[4] Ambs P. Optical computing: A 60-year adventure. Advances in Optical Technologies. 2010;**2010**:1-15

[5] Stone HS. Introduction to Computer Architecture. Chicago: Science Research Associates; 1975

[6] Akama S. Elements of Quantum Computing. New York: Springer Science+Business Media; 2015

[7] Gilmore CM. Introduction to Microprocessors. New York: McGraw-Hill; 1981

[8] Gaonkar RS. Microprocessor Architecture, Programming, and Applications with the 8085. New York: Prentice-Hall Inc.; 1999

[9] Sukhoivanov IA, Guryev IV. Photonic Crystals: Physics and Practical Modelling. New York: Springer; 2009

[10] Prather DW, Shi S, Murakowski J, Schneider GJ, Sharkawy A, Chen C, Miao B. Photonic crystal structures and applications: Perspective, overview, and development. IEEE Journal of Selected Topics in Quantum Electronics. 2006;**12**:1416-1437

[11] Joannopoulos JD, Meade RD, Winn JN. Photonic Crystals: Molding the Flow of Light. Princeton: Princeton University Press; 1995

[12] Notomi M, Shinya A, Mitsugi S, Kuramochi E, Ryu HY. Waveguides, resonators and their coupled elements in photonic crystal slabs. Optics Express. 2004;**12**:1551-1561

[13] Notomi M. Optical phenomena in photonic crystal. In: Noda S, Baba T, editors. Roadmap on Photonic Crystals. Boston: Kluwer Academic Publishers; 2003. p. 13-43

[14] Joannopoulos JD, Villeneuve PR, Fan S. Photonic crystals: Putting a new twist on light. Nature. 1997;**386**:143-149

[15] Kittel C. Introduction to Solid State Physics. 7th ed. New York: John Wiley & Sons; 1996

[16] Loncar M, Nedeljkovic D, Doll T, Vuckovic J, Scherer A, Pearsall TP. Waveguiding in planar photonic crystals. Applied Physics Letters. 2000;**77**:1937-1939

[17] Viktorovitch P. Physics of slow Bloch modes and their applications. In: Sibilia C, Benson TM, Marciniak M, Szoplik T, editors. Photonic Crystals: Physics and Technology. Milan: Springer; 2008. p. 27-42

[18] Liscidini M, Andreani LC. Photonic crystals: An introductory survey. In: Comoretto D, editor. Organic and Hybrid Photonic Crystals. New York: Springer; 2015. p. 3-30

[19] Tanabe T, Kuramochi E, Shinya A, Notomi M. Ultrahigh-Q photonic crystal nanocavities and their applications. In: Matsko A B, editor. Practical Applications of Microresonators in Optics and Photonics. Boca Raton: CRC Press; 2009. p. 1-52

[20] Notomi M. Manipulating light with strongly modulated photonic crystals. Reports on Progress in Physics. 2010;**73**:1-57

[21] Bogaerts W, Wiaux V, Taillaert D, Beckx S, Luyssaert B, Bienstman P, Baets R. Fabrication of photonic crystals in silicon-on-insulator using 248-nm deep UV lithography. IEEE Journal of Selected Topics in Quantum Electronics. 2002;**8**:928-934

[22] Prather DW, Sharkawy A, Shi S, Murakowski J, Schneider G, Chen C. Design and fabrication of planar photonic crystals. In: Kemme S, editor. Microoptics and Nanooptics Fabrication. Boca Raton: CRC Press; 2010. p. 151-189

[23] Levinson HJ. Principles of Lithography. 3rd ed. Bellingham: SPIE Press; 2010

[24] Loncar M, Scherer A. Microfabricated optical cavities and photonic crystals. In: Vahala K, editor. Optical Microcavities. Singapore: World Scientific; 2004. p. 39-93

[25] Griffiths DJ. Introduction to Electrodynamics. 3rd ed. New Delhi: Prentice-Hall; 1999

[26] Quimby RS. Photonics and Lasers: An Introduction. Hoboken: John Wiley & Sons; 2006

[27] Bründermann E, Hübers HW, Kimmitt MF. Terahertz Techniques. Berlin: Springer; 2012

[28] Fox M. Optical Properties of Solids. 2nd ed. New York: Oxford University Press; 2010

[29] Gai X, Choi DY, Madden S, Luther-Davies B. Materials and structures for nonlinear photonics. In: Wabnitz S, Eggleton BJ, editors. All-Optical Signal Processing: Data Communication and Storage Applications. New York: Springer; 2015. p. 1-33

[30] Golubev VG. Ultrafast all-optical switching in photonic crystals. In: Limonov MF, De La Rue RM, editors. Optical Properties of Photonic Structures: Interplay of Order and Disorder. Boca Raton: CRC Press; 2012. p. 415-428

[31] Tocci RJ, Widmer NS, Moss GL. Digital Systems: Principles and Applications. 10th ed. Upper Saddle River: Pearson Education; 2007

[32] Butcher PN, Cotter D. The Elements of Nonlinear Optics. Cambridge: Cambridge University Press; 1991

[33] Mano MM. Computer System Architecture. 3rd ed. New Delhi: Pearson Education; 1993

[34] Notomi M. Manipulating light by photonic crystals. NTT Technical Review. 2009;**7**:1-10

[35] Shinya A, Matsuo S, Tanabe T, Kuramochi E, Sato T, Kakitsuka T, Notomi M. All-optical on-chip bit memory based on ultra high Q InGaAsP photonic crystal. Optics Express. 2008;**16**:19382-19387

[36] Nozaki K, Shinya A, Matsuo S, Suzaki Y, Segawa T, Sato T, Kawaguchi Y, Takahashi R, Notomi M. Ultralow-power all-optical RAM based on nanocavities. Nature Photonics. 2012;**6**:248-252